10/16/95

SANDIA REPORT

SAND95–1905 • UC–814
Unlimited Release
Printed September 1995

Yucca Mountain Site Characterization Project

Pre-Test Simulations of Laboratory-Scale Heater Experiments in Tuff

Clifford K. Ho

Prepared by
Sandia National Laboratories
Albuquerque, New Mexico 87185 and Livermore, California 94550
for the United States Department of Energy
under Contract DE-AC04-94AL85000

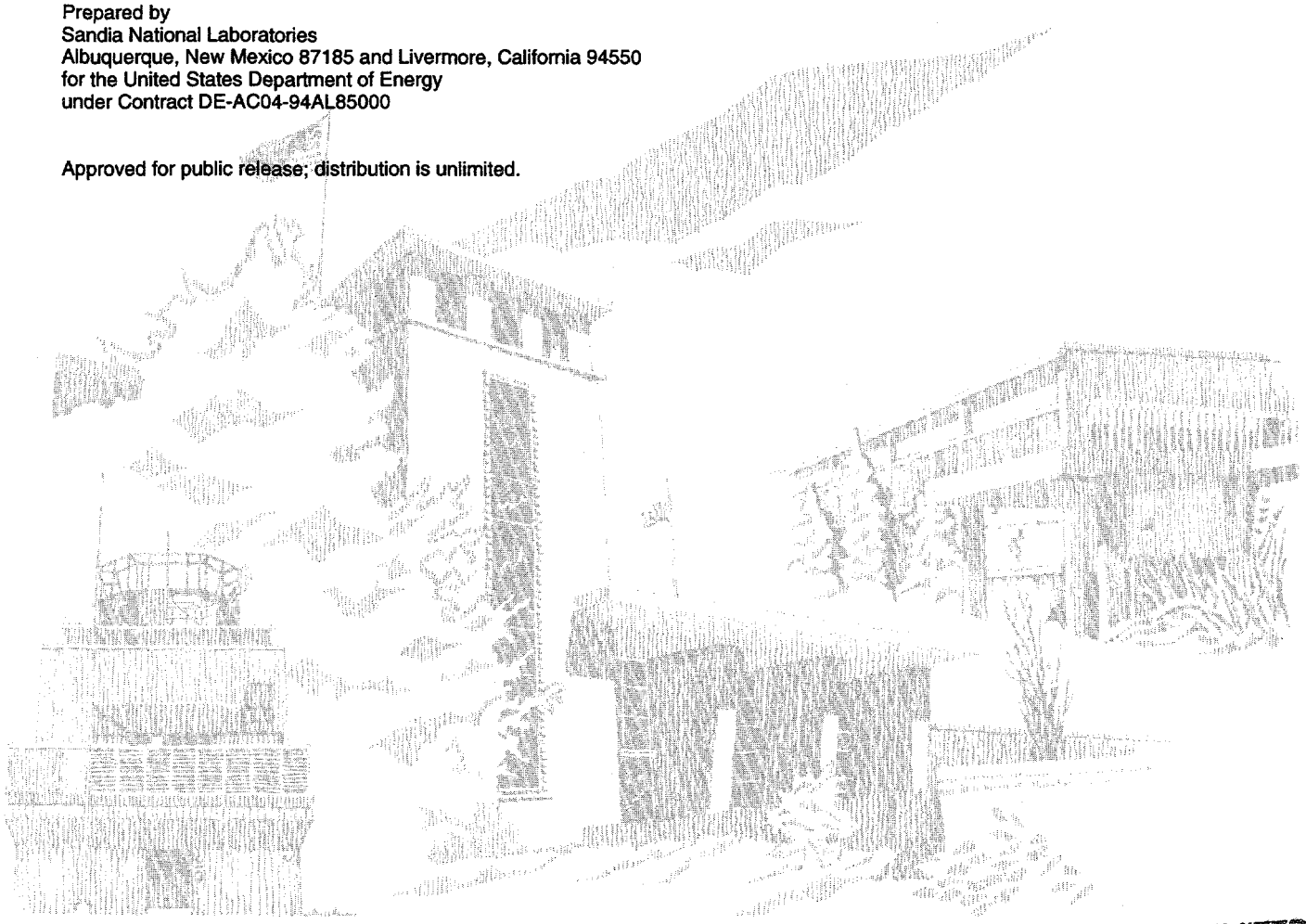

"Prepared by Yucca Mountain Site Characterization Project (YMSCP) participants as part of the Civilian Radioactive Waste Management Program (CRWM). The YMSCP is managed by the Yucca Mountain Project Office of the U.S. Department of Energy, DOE Field Office, Nevada (DOE/NV). YMSCP work is sponsored by the Office of Geologic Repositories (OGR) of the DOE Office of Civilian Radioactive Waste Management (OCRWM)."

Issued by Sandia National Laboratories, operated for the United States Department of Energy by Sandia Corporation.

Available to DOE and DOE contractors from
Office of Scientific and Technical Information
PO Box 62
Oak Ridge, TN 37831

Prices available from (615) 576-8401, FTS 626-8401

Available to the public from
National Technical Information Service
US Department of Commerce
5285 Port Royal Rd
Springfield, VA 22161

NTIS price codes
Printed copy: A04
Microfiche copy: A01

Distribution Category
UC-814

SAND95–1905
Unlimited Release
Printed September 1995

Pre-Test Simulations of Laboratory-Scale Heater Experiments in Tuff

Clifford K. Ho
Geohydrology Department
Sandia National Laboratories
Albuquerque, New Mexico 87185-1324

Abstract

Laboratory-scale heater experiments are proposed to observe thermohydrologic processes in tuffaceous rock using existing equipment and x-ray imaging techniques. The purpose of the experiments is to gain understanding of the near-field behavior and thermodynamic environment surrounding a heat source. As a prelude to these experiments, numerical simulations are performed to determine design-related parameters such as optimal heating power and heating duration. In addition, the simulations aid in identifying and understanding thermal processes and mechanisms that may occur under a variety of experimental conditions. Results of the simulations show that convection may play an important role in the heat transfer and thermodynamic environment of the heater if the Rayleigh-Darcy number exceeds a critical value (= 10 for the laboratory experiments) depending on the type of backfill material within the annulus (or drift).

PREFACE

This work was performed under the guidance of the US Department of Energy, Office of Civilian Radioactive Waste Management, Yucca Mountain Site Characterization Project, under contract #DE-AC04-94AL85000. The scientific investigation discussed in this report is covered under the description of work for WBS 1.2.5.4.6. The planning document that directed this work activity is WA-0040, Revision 02. None of the studies described in this report represent work that is defined as quality affecting.

ACKNOWLEDGMENTS

The author gratefully acknowledges Nick Francis, Steve Sobolik, and Peter Davies for their careful and thorough review of this report. The author also thanks Vince Tidwell for his insight and discussions of the laboratory experiments.

CONTENTS

LIST OF FIGURES

LIST OF TABLES

NOMENCLATURE

c_p	constant pressure specific heat (J/kg-K)
D_{va}	effective vapor-air diffusion coefficient in porous media
D^o_{va}	vapor-air diffusion coefficient
g	magnitude of gravity (m/s^2)
h	heat transfer coefficient (W/m^2-K)
k	permeability (m^2)
L_c	characteristic length (m)
m	mass (kg)
Nu	Nusselt number
P	gas pressure (Pa)
P_a	partial pressure of air in the gas-phase (Pa)
P_v	partial pressure of water vapor in the gas-phase (Pa)
P_{sat}	saturated vapor pressure (Pa)
q	heat flow rate (W)
q''	heat flux (W/m^2)
R	gas constant (J/kg-K)
Ra^*	Rayleigh-Darcy number
RH	relative humidity
RH^*	variation in relative humidity (Equation (3.13))
S	liquid saturation
S_g	gas saturation
T	temperature (K)
T^*	variation in temperature (Equation (3.12))
T_h	temperature of heater (K)
T_d	average temperature of the annulus wall (K)
$XAIR$	mass fraction of air in gas
$XVAP$	mass fraction of water vapor in gas
α	van Genuchten air-entry fitting parameter (1/Pa)
α_m	thermal diffusivity (m^2/sec)
β	van Genuchten fitting parameter; volumetric thermal expansion coefficient (K^{-1})
ϕ	porosity
λ	thermal conductivity (W/m-K)
ρ	density (kg/m^3)
ν	kinematic liquid viscosity (m^2/sec)
σ	Stefan-Boltmann constant (5.67×10^{-8} W/m^2-K^4)

θ	material parameter for effective diffusion coefficient
τ	tortuosity coefficient

Subscripts:

a	air
ave	denotes average value of elements directly above and below heater
above	denotes element directly above heater
below	denotes element directly below heater
r	radiative
v	vapor
f	fluid

Chapter

ONE

Introduction

1.1 Background

Studies of thermo-hydrologic flow processes have become increasingly important for assessing the performance of the potential high-level nuclear waste repository at Yucca Mountain. Emplacement of heat-generating wastes in the variably welded tuffs at Yucca Mountain may significantly impact the hydrologic behavior surrounding the repository. Previous studies have shown the possibility of buoyancy-driven convective cells (Tsang and Pruess, 1987), heat-pipe formation with counter-current liquid and vapor flow (Ho and Eaton, 1994; Pruess et al., 1990; Manteufel and Green, 1993), formation of condensation caps and refluxing (Pruess and Tsang, 1994; Buscheck and Nitao, 1993), and extended dry-out zones (Buscheck and Nitao, 1993) following the emplacement of heat-generating wastes at Yucca Mountain. These and other thermohydrologic processes may act favorably or unfavorably toward the isolation of waste from water and/or containment of radionuclides that leach from the waste packages. In addition, these processes will impact the environment in the drifts, which in turn will influence the containment performance of the waste packages. Studies by McNeish et al. (1995) and Gansemer and Lamont (1995) have stated that high temperatures (> 100°C) and low relative humidities (< 70%) are conducive to delaying the corrosion of the waste packages.

1.2 Problem Statement

Several experiments and field tests have been performed to investigate the thermohydrologic processes discussed above. Heater tests in G-Tunnel at Ranier Mesa were performed by several investigators including Johnstone et al. (1985) and Ramirez et al. (1990). In at least one of those tests, thermally induced water movement was evidenced by water accumulation in the heater holes.

However, definitive processes governing the water movement were inconclusive (Ho and Eaton, 1994). Laboratory-scale heater tests have also been performed by several investigators (Chen et al., 1995; Ho et al., 1994; Izzeldin et al., 1994; Manteufel and Green, 1993). Thermohydrologic processes such as heat-pipe (Manteufel and Green, 1993) and convective cells (Ho and Eaton, 1994) were observed in some laboratory experiments, but only unconsolidated materials were used. Similar experiments in tuffaceous rocks have yet to be performed. In Chen et al. (1995), temperature and relative humidity measurements were made in the annulus surrounding a heater element, but the measurements were made during a transient infiltration pulse through glass beads, which is not representative of the geologic media at Yucca Mountain. Capillary forces were very small relative to the gravity forces in that experiment as a result of the coarseness of the porous material that was used. In general, very few of the previous experiments and field tests have provided conclusive evidence or understanding of thermohydrologic flow processes and mechanisms that may occur at Yucca Mountain.

1.3 Overview and Purpose of the Report

This report proposes laboratory-scale heater experiments in actual tuff to address several of the issues described above. Proven capabilities developed in the Geohydrology Department at Sandia National Laboratories will allow the measurement of saturations in the tuff surrounding a heating element via x-ray imaging (Chapter 2). In addition, the temperature and relative humidity near the heater can be measured with and without an annulus. Different backfill materials can be used in the experiments within an annulus to determine the relative effects of convection, conduction, and radiation in the backfill. Numerical simulations are also presented in this report to determine important parameters relevant to the proposed experiments such as heater power, heating duration, and cool-down duration. These simulations are also performed to aid in understanding the thermohydrologic processes that will occur in the experiments. Chapter 3 presents the numerical approach, including a description of the code, the model domain, and parameters used in the simulations. Chapter 4 presents the results of the numerical simulations. Temperature and relative humidity values are presented as a function of heating duration and permeability of the annulus. Correlations between the Nusselt number and modified Rayleigh number are also presented to provide a general criterion for the significance of convection in various backfill materials.

Chapter

TWO

Laboratory Experiments

The proposed laboratory-scale experiments are based on existing experiments being performed in the Geohydrology Department at Sandia National Laboratories. X-ray imaging studies of liquid imbibition into slabs of tuff are currently being performed to investigate fracture-matrix interactions (Glass et al., 1994; Tidwell and Glass, 1992). The proposed experiments in this report will introduce a heater into the slab of tuff as shown in Figure 2.1. Transient saturations in the tuff can be recorded during heating and cool-down using the existing x-ray imaging technique and equipment. Temperatures and relative humidities can be recorded in the annulus using thermocouples and capacitance sensors as described in Chen et al. (1995). The annulus can be filled with different materials such as air, sand, or crushed rock, or the heater can be bored directly into the tuff with no annulus at all. Glass or Lexan panels are placed against the front and back of the tuff slab and secured to prevent evaporation and heat transfer across the face of the tuff slab. Temperature sensitive liquid crystals can be applied to one of the glass or Lexan panels to measure approximate temperatures throughout the tuff slab (Basel and Udell, 1991).

Fractures can be simulated by breaking a tuff slab and then reassembling the pieces between the glass or Lexan plates (Figure 2.2). Thermohydrologic processes in the presence of fractures can then be observed. However, the pre-test simulations presented in this report only consider a homogeneous tuff slab.

Several uncertainties exist with regards to the proposed experiments. First, significant heat loss may occur from the faces of the tuff slabs as experienced in previous non-isothermal experiments in a two-dimensional sand-filled apparatus (Ho et al., 1994). If additional insulation is applied to the Lexan or glass panels, they may need to be removed during the imaging of the saturations to prevent excessive exposure times. In addition, the ends of the tuff slab will probably be exposed to the atmosphere to prevent excessive pressure buildup. This allows vapor to escape

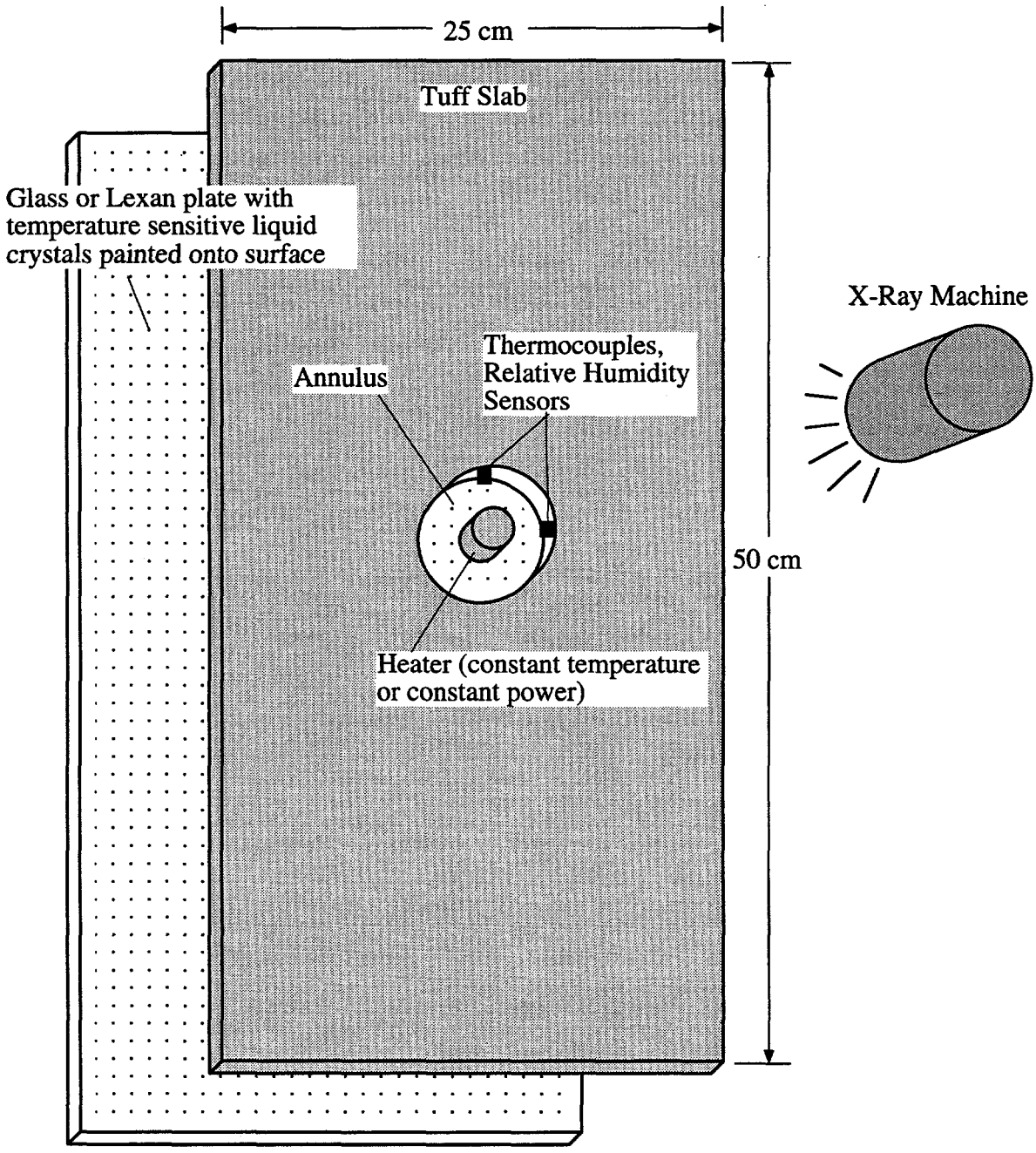

Figure 2.1. Sketch of the proposed laboratory-scale heater experiments with homogeneous tuff slab.

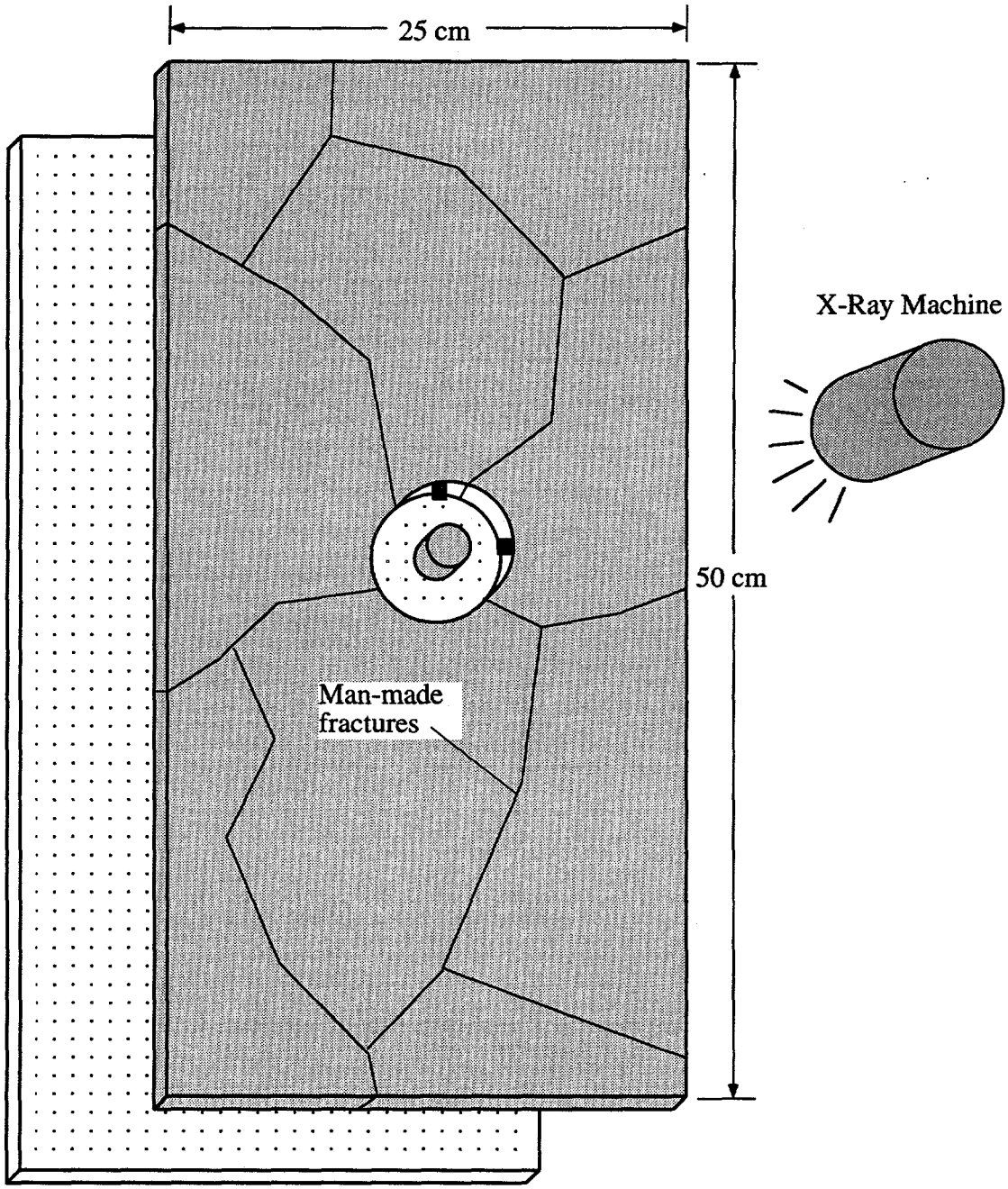

Figure 2.2. Sketch of the proposed laboratory-scale heater experiments with man-made fractures in the tuff slab.

with no convenient way to monitor the mass of water that is lost. Preferential pathways may also exist along the contact between the tuff slab and the panels through which vapor can escape. One solution might be to epoxy the panels onto the tuff slabs, but that would preclude the ease and repeatability of the experiments. The initial conditions will also be difficult to establish in the tuff slabs. The simulations in this report assume a constant saturation of 0.7 in the tuff slabs, but achieving a uniform saturation throughout the slabs may be difficult. Finally, the water used in the experiments must be doped (e.g. a potassium iodide solution) for use with the x-ray imaging. However, it is uncertain whether or not this solution will precipitate during heating. Previous experiments were performed under isothermal conditions and precipitation was not a problem.

Chapter

THREE

Numerical Approach

3.1 Numerical Model

The numerical code TOUGH2 (Pruess, 1991; Pruess, 1987) is a multiphase, nonisothermal, multidimensional numerical code that simulates the transport of air, water, and heat through porous media in both the gas and aqueous phases. TOUGH2 (SNL v. 3.2) is used to perform the pre-test simulations of the heater experiments to determine design-related parameters such as heater output power, heating duration, and cool-down duration. The simulations also aid in understanding thermohydrologic processes that may occur in the experiments.

The domain that is modeled with TOUGH2 is 25 cm wide x 50 cm high x 2.54 cm thick. The two-dimensional grid consists of 15 elements in the horizontal direction and 21 elements in the vertical direction (one element thick) with finer discretization in the middle (Figure 3.1). The element in the center represents the heater and is maintained at either a constant temperature or a constant wattage. The 5x5 grid of elements surrounding the heater element is used to represent the annulus†, and the remaining elements represent the tuff slab. The entire outer edge of the tuff slab is bordered by elements that represent air at constant temperature (20°C), pressure ($1x10^5$ Pa), and air mass fraction (1.0). Table 3.1 summarizes the properties and parameters used in the model along with the references.

The initial conditions for all the simulations assume a uniform temperature of 20°C. The liquid saturation in the tuff slab is assumed to be 0.7 while the saturation in the annulus (if one exists) is zero. The annulus is assumed to act as a capillary barrier; therefore, the liquid relative permeability is set to zero and the gas relative permeability is set to one in the elements comprising the annulus. Van Genuchten characteristic curves (1980) are used for the tuff slab, and the parameters are shown in Table 3.1

† In simulations with no annulus, the 5x5 grid assumes the same properties as the tuff slab.

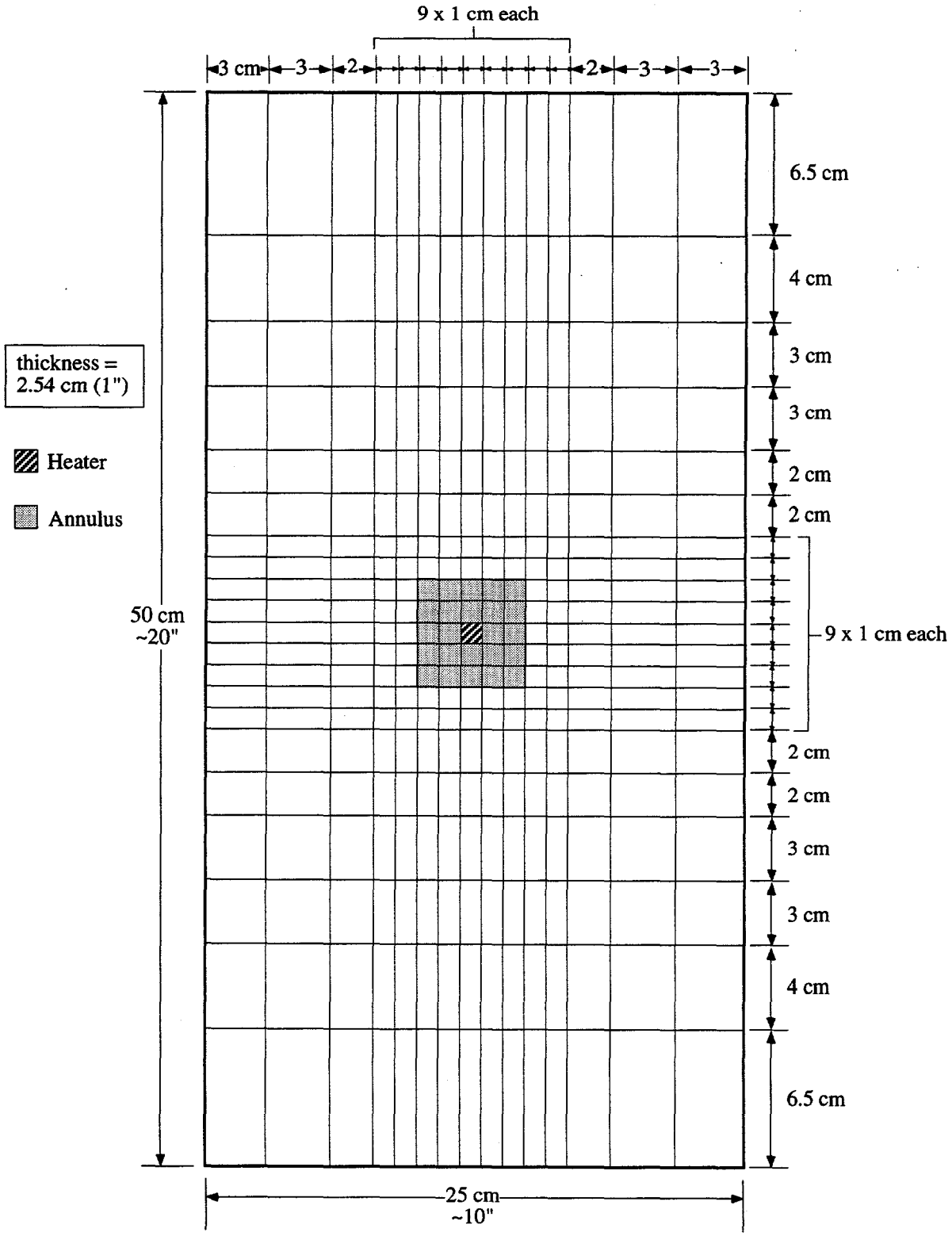

Figure 3.1. TOUGH2 mesh used in pre-test numerical simulations of laboratory-scale heater experiments.

Table 3.1. Model parameters used in TOUGH2 simulations.

	Tuff Slab	Heater	Annulus Materials		
			air	sand	crushed tuff
density (kg/m^3)	2480 (1)	8000 (4)	calculated in TOUGH2	2650 (6)	2600 (6)
porosity	0.2 (2)	0.0	1.0	0.41	0.45 (6)
permeability (m^2)	4.9×10^{-15} (2)	0.0	varies	varies	2.0×10^{-7} (6)
wet thermal conductivity (W/m-K) [1]	2.34 (1)	15.0 (4)	—	—	—
dry thermal conductivity (W/m-K)	1.9 (1)	15.0 (4)	0.4 (5)	0.4 (6)	0.6 (6)
specific heat (J/kg-K)	840 (1)	475 (4)	calculated in TOUGH2	717 (6)	840 (6)
van Genuchten α (1/Pa)	5.0×10^{-5} (2)	—	—	—	—
van Genuchten β	1.4	—	—	—	—
residual saturation	0.0453 (3)	—	—	—	—
comments	—	held at constant temperature (200 or 400°C) or constant power (5W)	The annulus materials maintained zero capillary pressure, a liquid relative permeability of zero, and a gas relative permeability of one. The initial air mass fraction was calculated to give a relative humidity of one (7).		

(1) Pruess and Tsang (1994), (2) Glass et al. (1994), (3) Wilson et al. (1994), (4) Incropera and DeWitt (1985), (5) see section 3.2.3, (6) Ho and Eaton (1994), (7) see section 3.2.2

3.2 Derivation of Physical Parameters

In this section, several important physical parameters that are used in the TOUGH2 model are explained and/or derived. These parameters consist of the effective vapor diffusion coefficient, the relative humidity as a function of air mass fraction, the effective thermal conductivity which includes radiation, the Nusselt and Rayleigh-Darcy numbers (Nield and Bejan, 1992), and parameters defining the variation in temperature and relative humidity near the heater.

3.2.1 Effective Vapor Diffusion Coefficient

The following equation defines the effective diffusion coefficient as used in TOUGH2:

$$D_{va} = \tau \phi S_g \frac{D^o_{va}}{P} \left(\frac{T + 273.15}{273.15} \right)^{\theta} \tag{3.1}$$

where D_{va} is the effective vapor-air diffusion coefficient in porous media, τ is the tortuosity coefficient, ϕ is the total porosity, S_g is the gas saturation, D^o_{va} is the vapor-air diffusion coefficient, P is the pressure, T is the temperature, and θ is a material parameter. In this study the vapor diffusion is assumed to be enhanced (Pruess and Tsang, 1993; Jury and Letey, 1979) such that the product of $\tau \phi S_g$ is equal to a constant value of 1.0. The values of D^o_{va} and θ are 2.14×10^{-5} m^2/sec and 2.334, respectively (Pruess and Tsang, 1994).

3.2.2 Relative Humidity and Air Mass Fraction

The primary variables that are used in TOUGH2 to account for the transport of air, water, and heat consist of gas pressure, gas saturation (two-phase) or air mass fraction (single-phase), and temperature. Since local thermodynamic equilibrium is assumed to exist within each element, the partial pressure of water will be equal to the saturated vapor pressure at the element temperature if the liquid saturation is greater than zero. However, if only a single-phase gas exists in an element, then the air mass fraction is used to specify the relative amounts of air and water in the gas phase in the element. This section derives a relation between the relative humidity and air mass fraction, which is used to determine relative humidities presented in Chapter 4.

The definitions of the relative humidity, RH, and air mass fraction, XAIR, are given in equations (3.2) and (3.3):

$$RH = \frac{P_v}{P_{sat}(T)} \tag{3.2}$$

$$XAIR = \frac{m_a}{m_a + m_v} = \frac{1}{1 + \frac{m_v}{m_a}} \tag{3.3}$$

where P_v is the partial pressure of vapor, $P_{sat}(T)$ is the saturation vapor pressure at temperature, T, m is the mass of a component in the gas phase, and the subscripts a and v denote the air and water vapor components, respectively. Assuming the gas is ideal, the ideal gas law is used in equation (3.3) to yield the following expression for the air mass fraction as a function of the partial pressures of air and vapor:

$$XAIR = \frac{1}{1 + \frac{P_v}{P_a}\frac{R_a}{R_v}} \tag{3.4}$$

where R_a is the gas constant for air (=287.0 J/kg-K) and R_v is the gas constant for water vapor (=461.52 J/kg-K). The sum of the partial pressures equals the total gas pressure, so the partial pressure of air can be expressed as $P_a = P - P_v$. Using this substitution, equation (3.4) can be rearranged to solve for the partial pressure of water vapor as a function of air mass fraction and total gas pressure:

$$P_v = \frac{P}{\left(\frac{XAIR}{1 - XAIR}\right)\frac{R_a}{R_v} + 1} \tag{3.5}$$

Equation (3.5) can be used in equation (3.2) to determine the relative humidity of any element as a function of air mass fraction, pressure, and temperature. Conversely, equation (3.4) can be used with equations (3.2) and (3.5) to determine the air mass fraction when the relative humidity, pressure, and temperature are known. This is useful for initializing elements in TOUGH2 if the relative humidity is specified. In the simulations presented in Chapter 4, this procedure was performed to calculate the initial air mass fraction of the elements in the annulus corresponding to a relative humidity of one, a pressure of 1×10^5 Pa, and a temperature of 20°C. It should also be noted that the sum of the air mass fraction, XAIR, and the vapor mass fraction, XVAP, equals one.

3.2.3 Effective Thermal Conductivity with Radiation

Radiation was not explicitly considered in the simulations performed in this report. In backfill materials such as sand and crushed tuff, radiation is not expected to be significant at the temperatures of interest. However, radiation may play a dominant role in transporting heat through an annulus filled with air. Therefore, the effective thermal conductivity of air was enhanced to

account for radiative effects in the annulus. Assuming the radiation from the heater, q_r, to the surrounding tuff behaves as blackbody radiation with no participation from the air, the following equation describes the heat flow from the heater to the surrounding tuff:

$$q_r = \sigma\left(T_h^4 - T_d^4\right) \tag{3.6}$$

where σ is the Stefan-Boltzmann constant (=5.67x10^{-8} W/m^2-K^4), T_h is the temperature of the heater, and T_d is the average temperature of the annulus wall. Expanding equation (3.6) yields the following expression in terms of a radiation heat transfer coefficient, h_r:

$$q_r = h_r\left(T_h - T_d\right)$$

where

$$h_r = \sigma\left(T_h + T_d\right)\left(T_h^2 + T_d^2\right) \tag{3.7}$$

In TOUGH2, the heat transfer coefficient must be written in terms of an effective thermal conductivity. Assuming that quasi-steady conditions exist in the air annulus (linear temperature profile), the effective radiative conductivity of air, λ_r, can be written as follows:

$$\lambda_r = h_r \Delta x = \sigma\left(T_h + T_d\right)\left(T_h^2 + T_d^2\right)\Delta x \tag{3.8}$$

where Δx is the distance between the heater and the annulus wall (= 2 cm). Since most of the simulations presented in Chapter 4 use a constant heater temperature of 200°C (473 K), two extreme radiative conductivities are calculated with equation (3.8) using annulus wall temperatures of 20°C and 200°C to yield 0.25 W/m-K and 0.48 W/m-K, respectively. These conductivities are then averaged to yield an effective radiative conductivity of 0.37 W/m-K. The radiative conductivity is added to the normal thermal conductivity of air at 350K (= 0.03 W/m-K (Incropera and DeWitt, 1985)) to yield an effective thermal conductivity of 0.4 W/m-K for air as shown in Table 3.1. Several major assumptions have been made in this derivation, most notably the invariance of the thermal conductivity with temperature, and should be viewed as limitations.

3.2.4 Nusselt and Rayleigh-Darcy Numbers

A primary objective of the pre-test simulations is to identify processes that may play an important role in the thermohydrologic behavior of the experiments. Natural convection in the annulus is suspected to be a potential mechanism to enhance heat transfer and cause variations in temperature and relative humidity around the heater. This may have implications for the containment performance of heat-generating waste packages in a drift. In order to characterize the relative effect of natural convection in porous media, the Nusselt, *Nu*, and Rayleigh-Darcy, *Ra**,

numbers are often used (Nield and Bejan, 1992). The Nusselt number is a measure of the amount of convective heat transfer relative to conductive heat transfer. The Rayleigh-Darcy number is a ratio of the buoyancy forces to viscous forces in a porous medium. Both numbers are defined as follows:

$$Nu = \frac{h L_c}{\lambda} = \frac{q''}{\left(T_h - T_d\right)} \frac{L_c}{\lambda} \tag{3.9}$$

$$Ra^* = \frac{g \beta \left(T_h - T_d\right) k L_c}{\nu \alpha_m} \tag{3.10}$$

where q'' is the heat flux from the heater to the annulus wall, L_c is a characteristic length (= height of the annulus = 0.05 m), λ is the effective thermal conductivity of the annulus material (and fluid), g is the magnitude of the gravity vector, β is the volumetric thermal expansion coefficient (= $1/T$ for ideal gas), k is the permeability of the annulus, ν is the kinematic viscosity of the fluid in the annulus, and α_m is defined below:

$$\alpha_m = \frac{\lambda}{\left(\rho c_p\right)_f} \tag{3.11}$$

where $(\rho c_p)_f$ is the heat capacity of the *fluid* in the annulus. In quasi-steady systems in which the temperatures are not changing rapidly, the time-dependent terms in the energy equation, which contain the heat capacity of the solid phase, are dropped. Thus, the thermal diffusivity given in equation (3.11) is a function of the fluid heat capacity, which is retained in the convective components in the energy equation.

All of the material properties in equations (3.9)–(3.11) are evaluated at a mean of the heater and annulus wall temperatures. The annulus wall temperature is taken to be an average of the temperatures of the elements surrounding the annulus. Figure 3.2 shows a worksheet that is used to calculate these parameters for a sample simulation. These parameters are presented in Chapter 4 for all of the numerical simulations.

One last note should be made regarding the simulation of an air annulus. Rigorously speaking, Darcy's law cannot be used to determine the velocity distribution caused by natural convection in an open air annulus. Inertial terms in the full Navier-Stokes equation are neglected in Darcy's law and may play an important role in the velocity distribution. However, in this study, these effects are lumped into Darcy's law using an effective permeability (several orders of

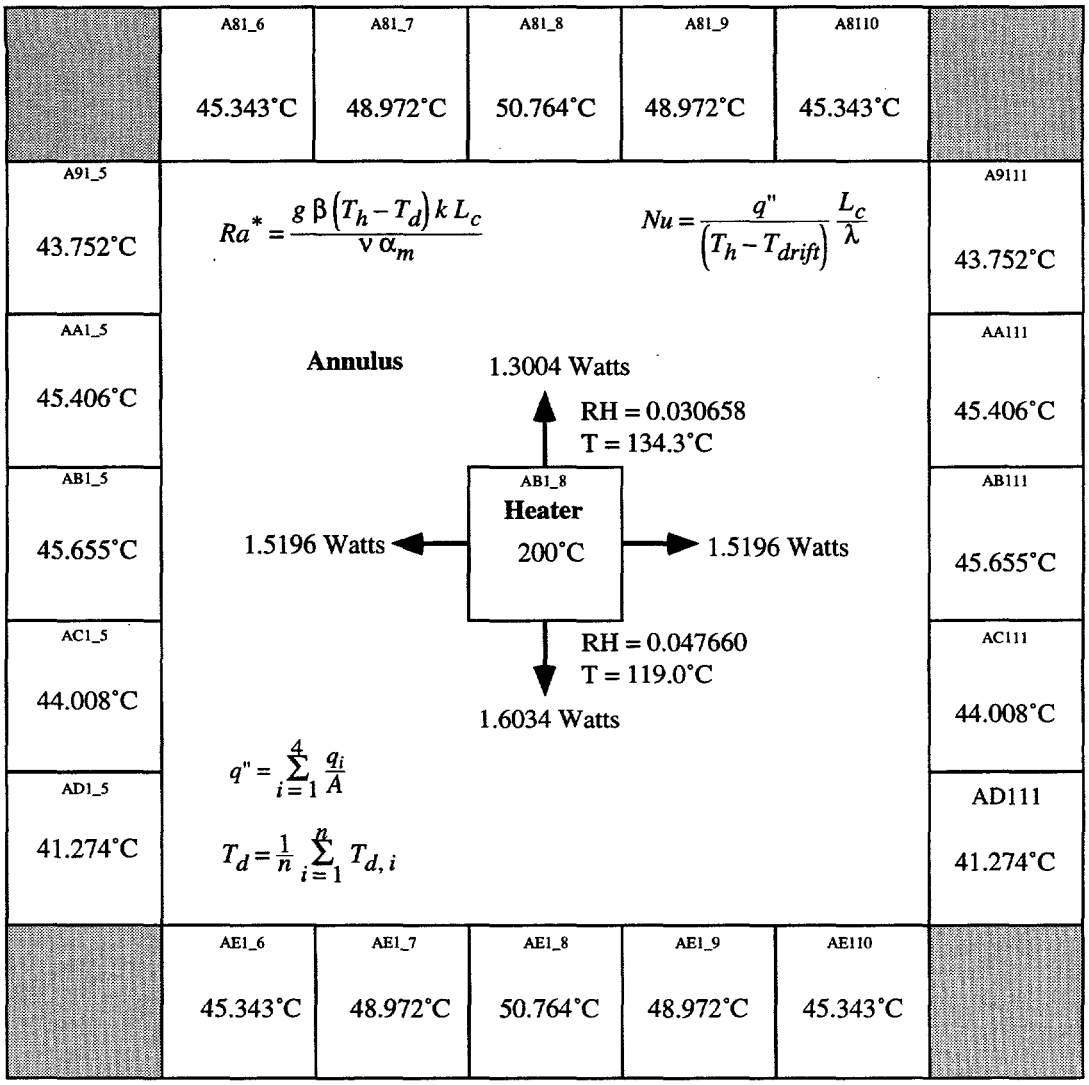

$q'' = (1.3004+1.5196+1.5196+1.6034)/0.0254m^2 = 234\ W/m^2$
$T_d = 44.483°C$
$T_{ave} = (200 + 44.483)/2 = 122°C = 395\ K$
$\rho_f(395K) = 0.8829\ kg/m^3$
$c_{p,f}(395K) = 1.014e3\ J/kg\text{-}K$
$\nu_f(395K) = 2.589e\text{-}5\ m^2/sec$
$\alpha_m(395K) = 4.468e\text{-}4\ m^2/sec$
$\beta = 1/T_{ave} = 2.53e\text{-}3\ K^{-1}$
Incropera and DeWitt (1985)
$L_c = 0.05\ m$

Ra* = 33.37
Nu = 0.1881
T* = 0.1209
RH* = 0.4342

Figure 3.2. Sample worksheet to calculate Rayleigh-Darcy number, Ra*, Nusselt number, Nu, variation in temperature, T*, and variation in relative humidity, RH*. The temperatures of the annulus wall, the heater temperature, and the heat fluxes were output from TOUGH2 after 1 day for a simulation using an "air" annulus with a permeability of $2x10^{-6}$ m^2 and effective thermal conductivity of 0.4 W/m-K.

magnitude higher than other porous materials) for the air annulus†. Under these conditions, the air is essentially being modeled as a porous material. The results in Chapter 4 will show that since the effective thermal conductivities of the air and sand are equal (Table 3.1), the Nusselt and Rayleigh-Darcy numbers are the same for simulations using the same heater temperature but different annulus materials (either air or sand) under quasi-steady conditions (recall that the heat capacity of the solid does not play a role in the energy equation under quasi-steady conditions).

3.2.5 Variations in Temperature and Relative Humidity Near the Heater

In addition to the Nusselt and Rayleigh-Darcy numbers, the variation in temperatures and relative humidities near the heater are indicators of the effects of convection. The system being modeled can establish counter-rotating convective cells (Ho and Eaton, 1994) that cause the temperature just above the heater to be higher than the temperature just below the heater if convection is significant. Subsequently, the relative humidity just above the heater will be lower than the relative humidity just below the heater. In order to quantify these variations, the following expressions are given for the variation in temperature, T*, and the variation in relative humidity, RH*:

$$T^* = \frac{T_{above} - T_{below}}{T_{ave}} = \frac{T_{above} - T_{below}}{\frac{\left(T_{above} + T_{below}\right)}{2}} \tag{3.12}$$

$$RH^* = \frac{RH_{above} - RH_{below}}{RH_{ave}} = \frac{RH_{above} - RH_{below}}{\frac{\left(RH_{above} + RH_{below}\right)}{2}} \tag{3.13}$$

where the subscripts *above* and *below* refer to the elements just above and below the heater, and the subscript *ave* refers to the average value of those two elements. The variations in temperature and relative humidity are plotted as a function of the Rayleigh-Darcy number in Chapter 4.

† In this particular problem, an upper bound for the permeability can be calculated by assuming Poiseuille flow through parallel planes separated by a distance, b. If b is set equal to the thickness of the tuff slab, then the upper bound on the permeability can be estimated to be 5×10^{-5} m^2 ($=b^2/12$).

Chapter

FOUR

Numerical Results

4.1 Overview of Numerical Simulations

The TOUGH2 model described in the previous chapter is used to simulate the laboratory-scale heater experiments under a variety of conditions. Various materials are simulated as backfill for the annulus including air, sand, and crushed tuff. The temperature of the heater is varied between simulations, and in some of the simulations the heater is maintained at a constant wattage instead of temperature. Table 4.1 summarizes the simulations that are performed and reported in this chapter. The heating and cool-down durations that are listed are sometimes dictated by the maximum number of time steps allotted for each simulation (4000). It should also be noted that the cool-down periods for simulations with a constant temperature heater were simulated by physically removing the heater. In the cool-down periods for a constant wattage heater, the cool-down was simulated by turning the heater power off but leaving the element in place. The purpose of performing such a wide variety of simulations is to bound the thermohydrologic processes that may occur in the actual laboratory experiments. Extensions to field-scale behavior and processes can also be made by compiling the wide range of data into meaningful non-dimensional parameters that are independent of scale (section 4.4).

4.2 Visualization of Thermohydrologic Processes

In this section, two simulations (1 & 3B) are analyzed for the purpose of visualizing thermohydrologic processes that may occur under a variety of conditions in the laboratory heater experiments. The first simulation yields results when the heater is placed directly into the tuff slab with no annulus. The second simulation presents results when a sand-filled annulus surrounds the heater as shown in Figure 3.1.

Table 4.1. Summary of TOUGH2 numerical simulations.

Simulation	Heat Load Type	Annulus Material	Annulus Permeability	Heating Duration	Cool-Down Duration
1	T_h=200°C	no annulus*	—	1 day	3 days†
2A	T_h=200°C	air	$1x10^{-5}$ m^2	17 hours	—
2B	T_h=200°C	air	$5x10^{-6}$ m^2	1 day	—
2C	T_h=200°C	air	$2x10^{-6}$ m^2	1 day	—
2D	T_h=200°C	air	$1x10^{-6}$ m^2	1 day	1.2 days†
2E	q = 5 Watts	air	$1x10^{-6}$ m^2	1 day	1.6 days††
2F	T_h=400°C	air	$1x10^{-6}$ m^2	1 day	—
2G	T_h=200°C	air	$1x10^{-7}$ m^2	1 day	—
2H	T_h=200°C	air	$7.3x10^{-10}$ m^2	1 day	—
3A	T_h=200°C	sand	$1x10^{-5}$ m^2	6 hours	—
3B	T_h=200°C	sand	$7.3x10^{-10}$ m^2	1 day	3 days†
3C	T_h=400°C	sand	$7.3x10^{-10}$ m^2	1 day	—
3D	q = 5 Watts	sand	$7.3x10^{-10}$ m^2	1 day	3 days††
4	T_h=200°C	crushed tuff	$2x10^{-7}$ m^2	1 day	—

†The cool-down period was simulated by physcially removing the heater element from the model.
††The cool-down period was simulated by turning the heater power off, but leaving the element in place.
*The heater was placed directly into the tuff.

4.2.1 Visualization of Simulation 1 with No Annulus

Figure 4.1 shows the liquid- and gas-phase velocities superposed on top of the liquid saturations in a region around the heater after 6 hours of heating with a constant heater temperature of 200°C and no annulus (simulation 1). The region that is shown corresponds to the 9 x 9 uniform elements surrounding the heater as shown in Figure 3.1. An evaporation front coincident with the perimeter of a dry region grows outward from the heater. The liquid velocities outside of this dry region are directed toward the heater as a result of capillary suction towards the lower saturations. The gas velocities are directed outwards from the heater and are greatest near the evaporation front approximately 3 cm outside of the heater. The evaporation of the liquid water increases the pressure in that region, creating pressure gradients that advectively drive the water vapor and air away from the heater. Although not shown, the water vapor mass fraction is greatest near this evaporation front and decreases away from the front in either direction. This implies that vapor diffusion is directed both towards and away from the heater near the evaporation front. However, the gradient in the vapor mass fraction is largest in the direction away from the heater.

Figure 4.2 shows the temperature and relative humidity contours superposed on top of the liquid saturations at 6 hours for simulation 1. The temperatures decrease from 200°C at the heater to around 100°C at the evaporation front. Since vapor pressure lowering is neglected in this study, the boiling point of water in situ corresponds closely to 100°C at the system pressure. Thus, the evaporation (or drying) front is located near where boiling of the liquid occurs. The relative humidity is one near the evaporating surface and wherever water is present. The relative humidity decreases towards the heater as a result of the higher temperatures that increase the saturated vapor pressure of water above the existing partial vapor pressures (see equation 3.2).

4.2.2 Visualization of Simulation 3B with a Sand Annulus

Simulation 3B is analyzed after 6 hours of heating with a constant heater temperature of 200°C. A sand-filled annulus exists around the heater as shown in Figure 3.1. The liquid velocities are directed toward the annulus in the surrounding tuff slab as shown in Figure 4.3, but no liquid enters the annulus as a result of the imposed zero liquid relative permeability of the annulus (section 3.1). These velocities are small compared to the liquid velocities in the previous simulation with no annulus. In this case, the saturation (and hence capillary pressure) gradients around the annulus are small, which cause the capillary-driven liquid velocities to be small as well. The gas-phase velocities are seen to be greatest within the sand-filled annulus (Figure 4.3) and take the form of buoyancy induced counter-rotating convective cells. However, the magnitudes of

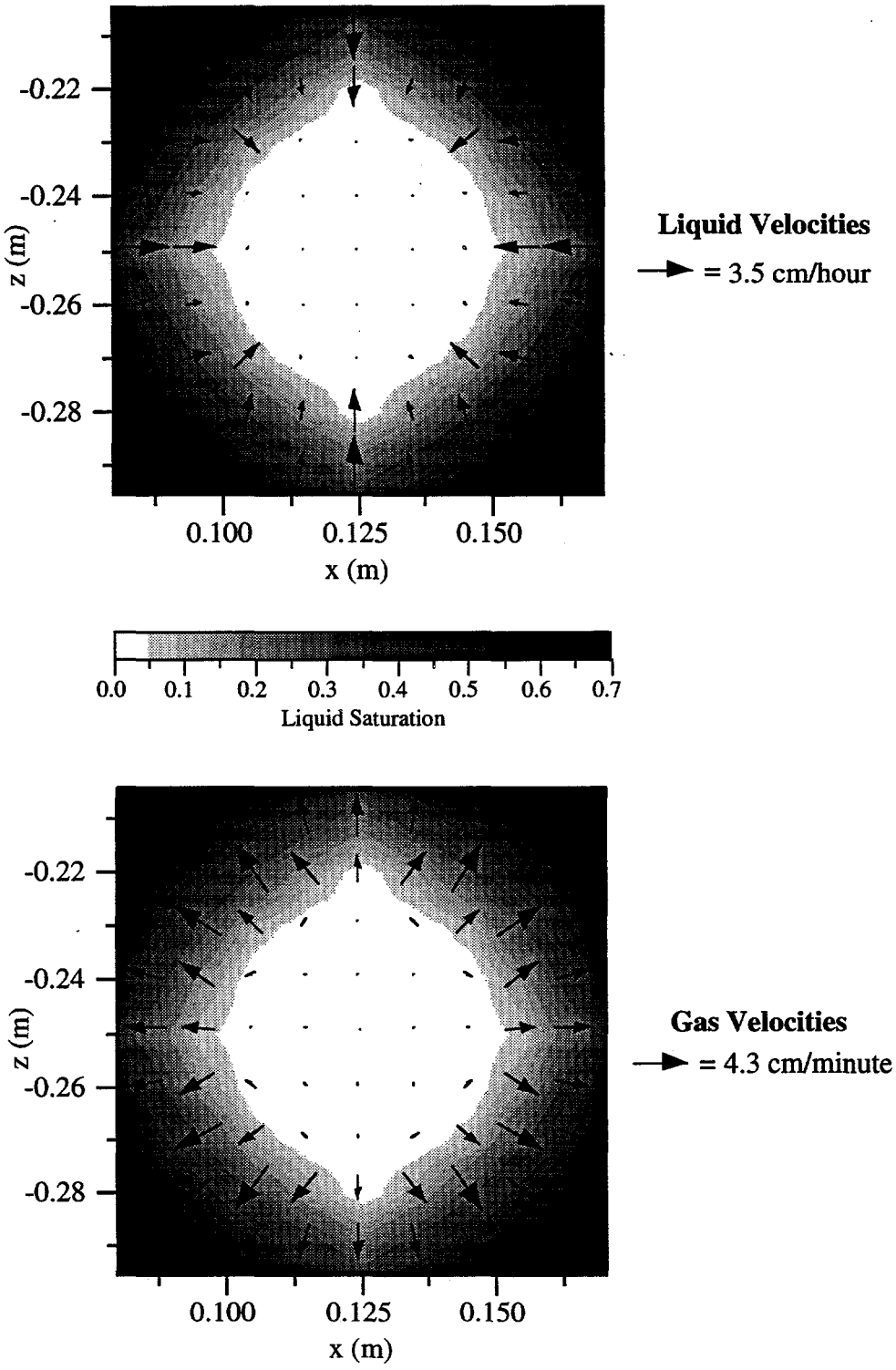

Figure 4.1. Liquid- and gas-phase velocities superposed on top of the liquid saturations after 6 hours of heating with a constant temperature of 200°C in a region surrounding the heater (9x9 uniform elements). No annulus is used in this simulation (run 1).

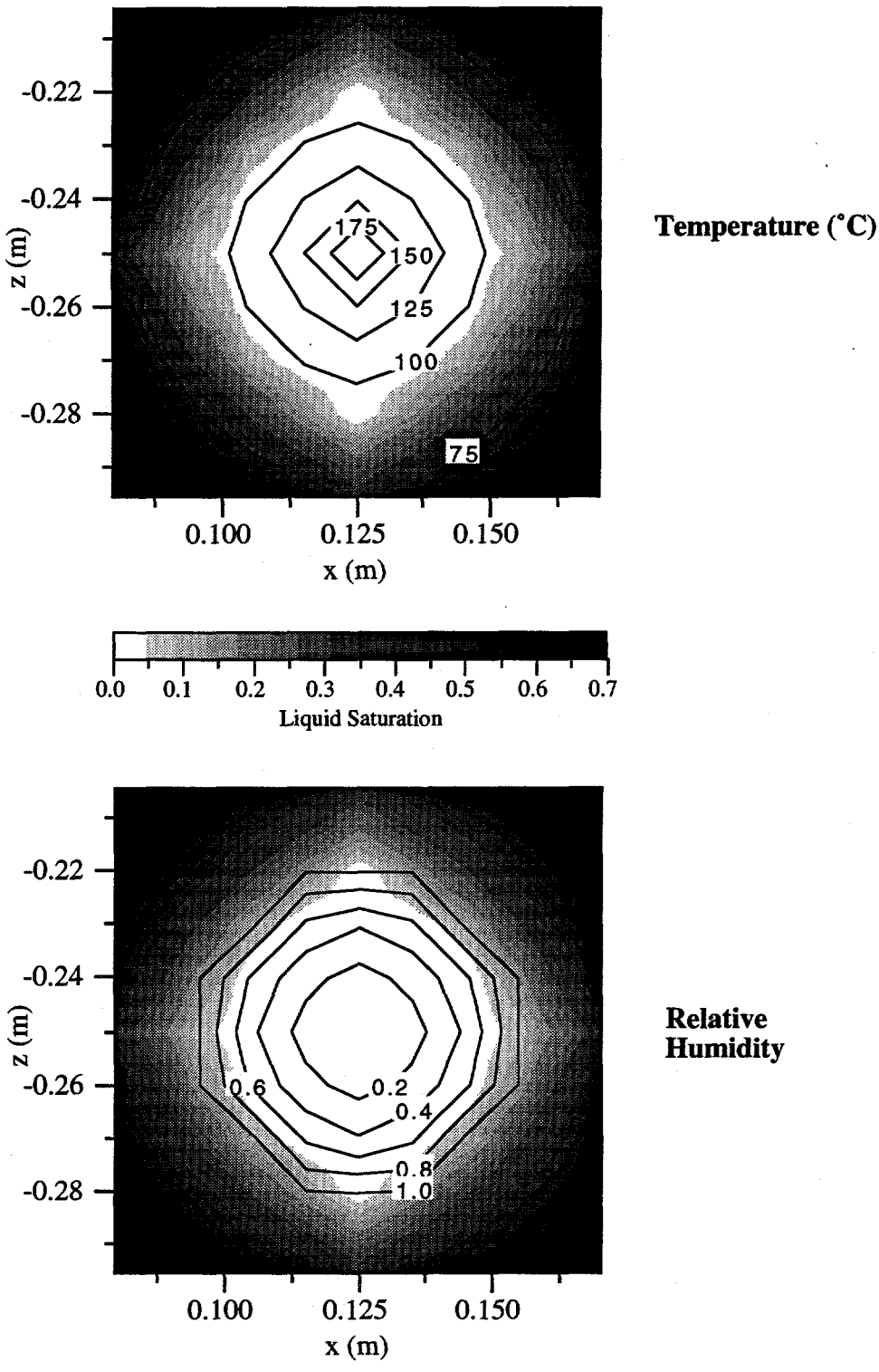

Figure 4.2. Temperature and relative humidity contours superposed on top of the liquid saturations after 6 hours of heating with a constant temperature of 200°C in a region surrounding the heater (9x9 uniform elements). No annulus is used in this simulation (run 1).

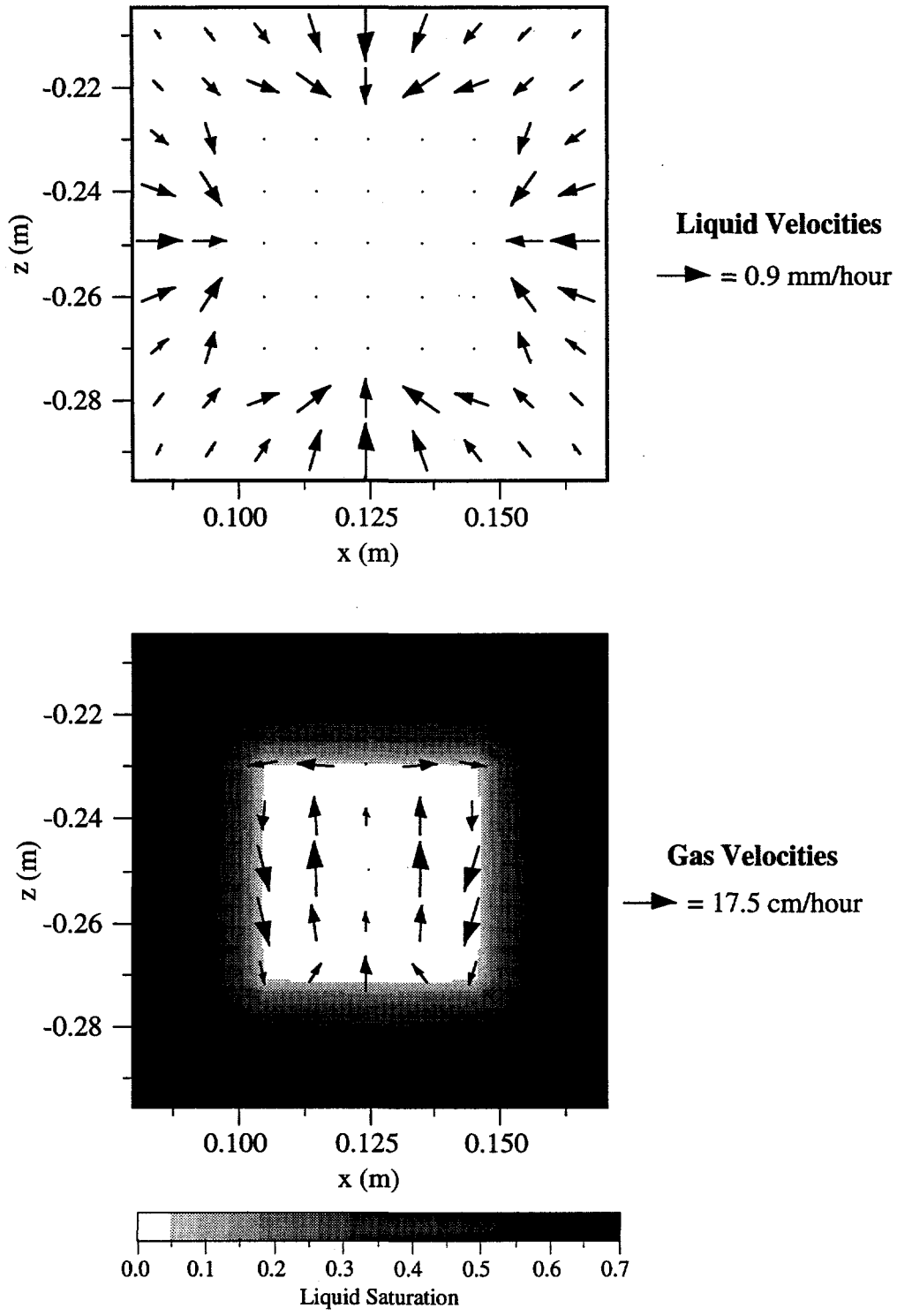

Figure 4.3. Liquid- and gas-phase velocities after 6 hours of heating with a constant temperature of 200°C in a region surrounding the heater (9x9 uniform elements) with a sand-filled annulus (simulation 3B). The liquid saturations are also shown with the gas velocities.

these gas velocities are quite small (17.5 cm/hour) and are not expected to affect the thermohydrologic parameters of the system.

The temperature and relative humidity contours are superposed on top of the liquid saturations in Figure 4.4 for simulation 3B. Note that the temperatures and relative humidities are uniformly distributed around the heater, confirming that convection does not play a significant role in this case. The temperatures are generally less than the previous case with no annulus, and the relative humidities are also less near the heater.

4.2.3 Visualization of Simulation 2A with an Air Annulus

Simulation 2A is similar to simulation 3B except that the permeability specified for the air-filled annulus is over four orders of magnitude higher than the sand-filled annulus. Figure 4.5 shows the liquid- and gas-phase velocities after 6 hours of heating with a constant temperature of 200°C. The gas velocities are seen to be several orders of magnitude higher in the annulus than in the previous case. As a result, the nature of the upward flow of hot air in the center of the annulus tends to dry out the top part of the annulus more quickly than other locations as shown in Figure 4.5. This dry-out region near the top wall of the annulus subsequently creates capillary pressure gradients that cause liquid to flow towards the drier regions along the top wall of the annulus. The magnitudes of the liquid velocities are on the same order as the liquid velocities in simulation 1 with no annulus.

Figure 4.6 shows that the resulting temperature and relative humidity contours are non-uniform about the heater. The high permeability of the annulus in this simulation allows the convection to significantly alter the temperatures and relative humidities. In general, the temperatures above the heater are higher as a result of the upward flow of heated air near the center of the annulus. The shape of the relative humidity contours are nearly opposite the shape of the temperature contours as a result of the inverse relationship between relative humidity and temperature (equation (3.2)).

To quantify the saturation distribution in Figures 4.5 and 4.6, the saturations along a vertical transect through the center of the domain are plotted in Figure 4.7. For comparison, the saturations in the previous two simulations are shown as well. The saturations near the bottom of the domain with the air annulus exceed the initial saturation of 0.7, indicating a condensation rate that exceeds the evaporation in that location. This behavior appears to be accentuated by the convection within the annulus. It is hypothesized that the counter-rotating convective cells act to volatilize more water near the top of the annulus where the temperatures are higher. This moisture-

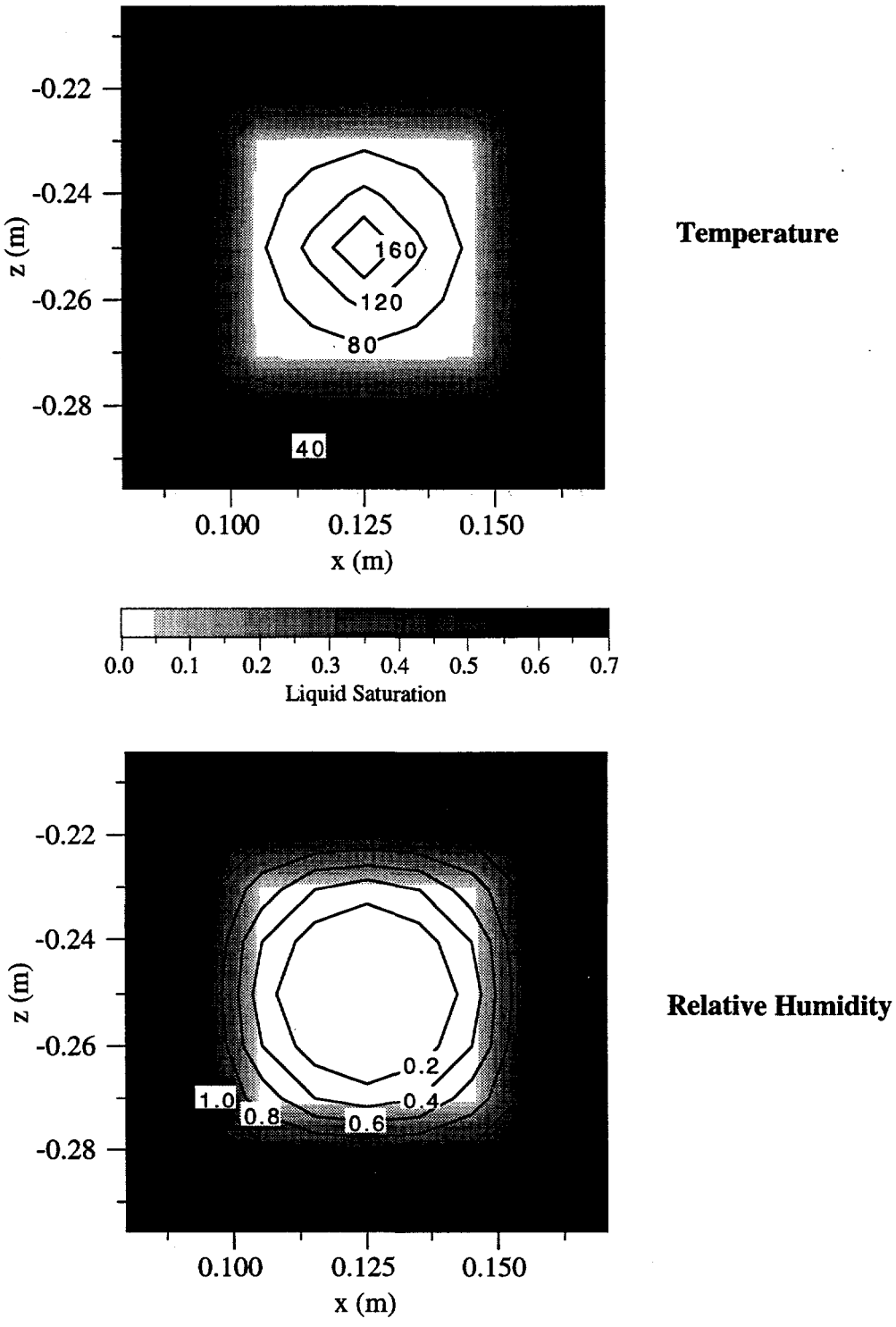

Figure 4.4. Temperature and relative humidity contours superposed on top of liquid saturations after 6 hours of heating with a constant temperature of 200°C in a region surrounding the heater (9x9 uniform elements) with a sand-filled annulus (simulation 3B).

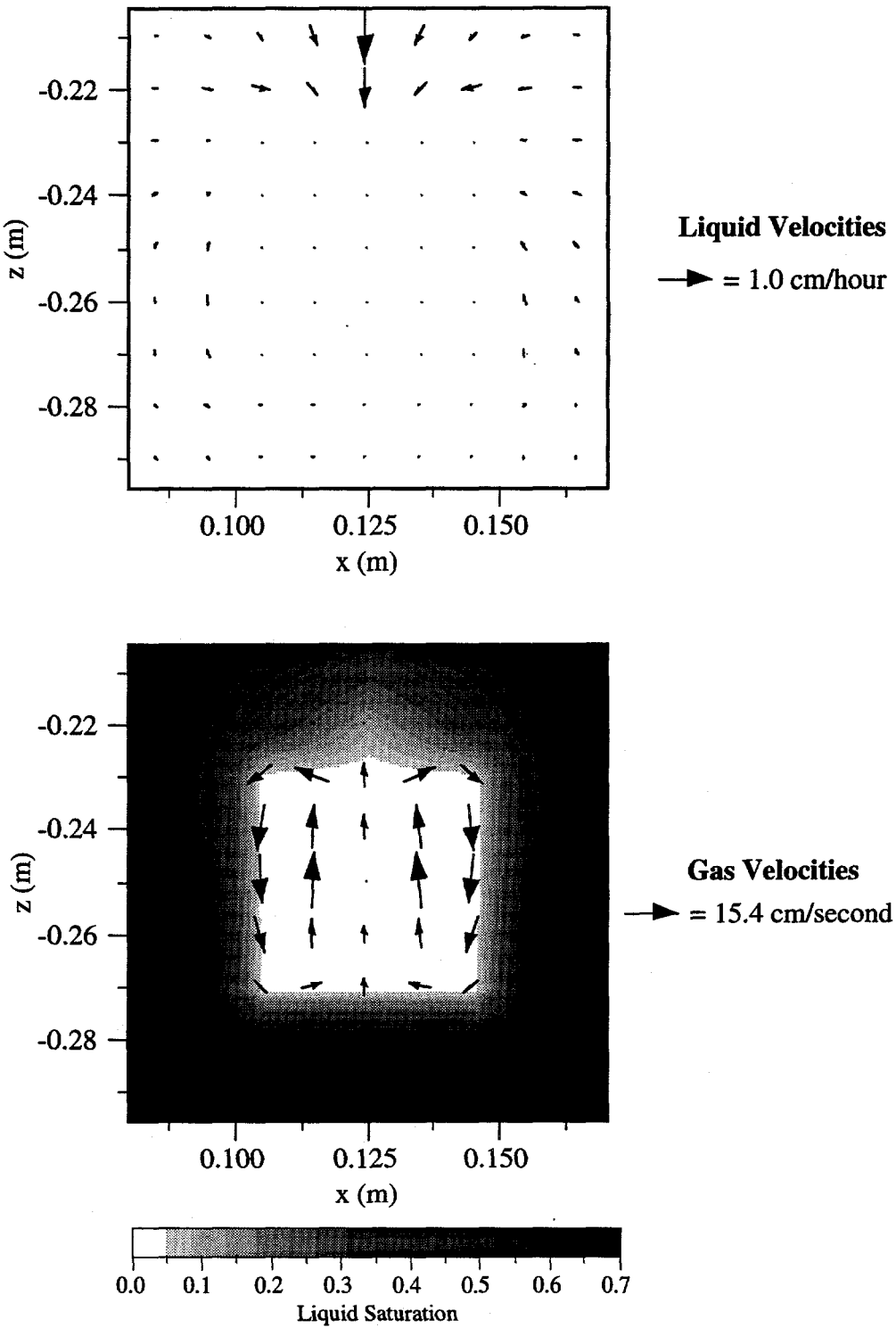

Figure 4.5. Liquid- and gas-phase velocities after 6 hours of heating with a constant temperature of 200°C in a region surrounding the heater (9x9 uniform elements) with an air-filled annulus (simulation 2A). The liquid saturations are also shown with the gas velocities.

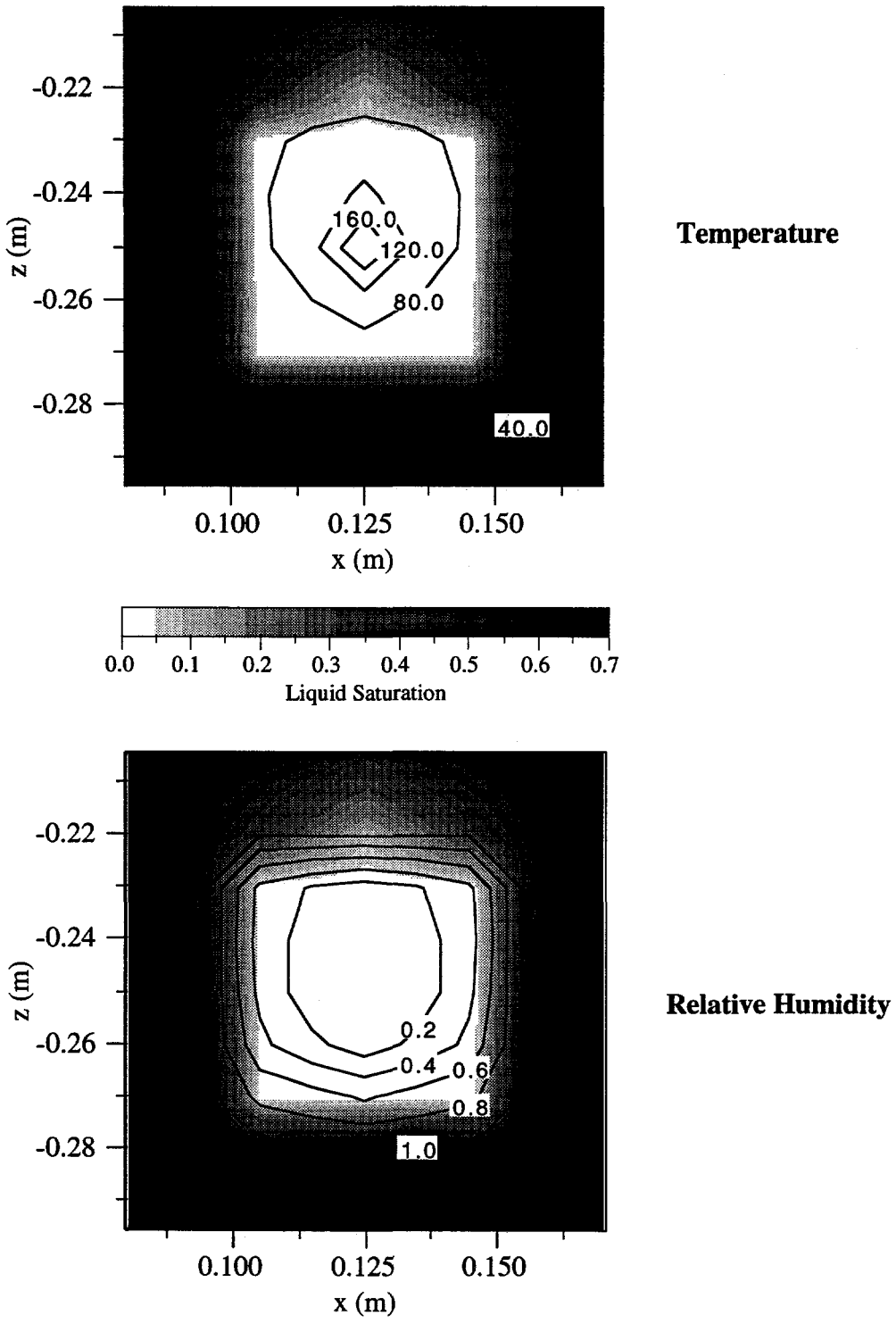

Figure 4.6. Temperature and relative humidity contours superposed on top of liquid saturations after 6 hours of heating with a constant temperature of 200°C in a region surrounding the heater (9x9 uniform elements) with an air-filled annulus (simulation 2A).

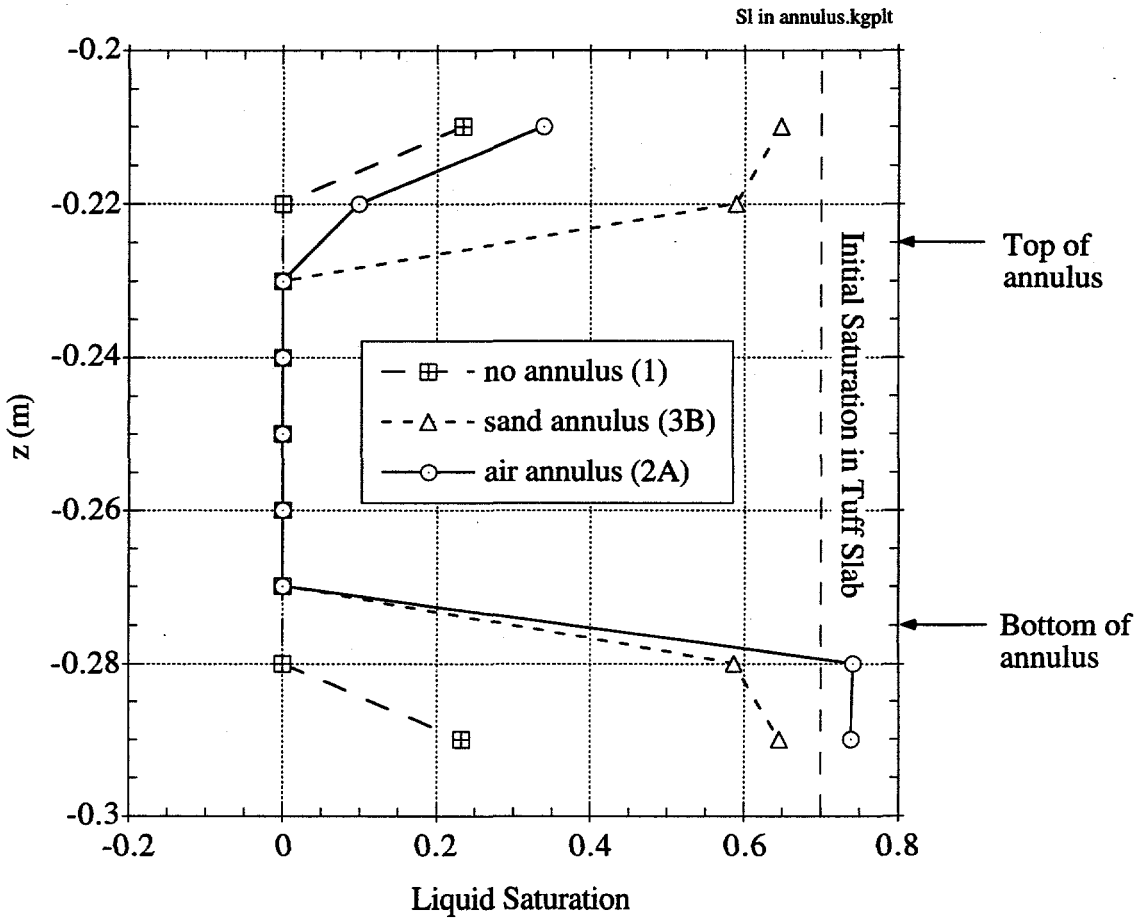

Figure 4.7. Saturations along a vertical transect through the center of the annulus for simulations with no annulus (1), a sand annulus (3B), and an air annulus (2A) after 6 hours of heating with a constant heater temperature of 200°C.

laden gas then flows downward along the outside of the annulus where it cools, thereby condensing the liquid toward the bottom of the annulus. Therefore, at early times, convection may act to redistribute moisture from the top of the annulus (or drift wall) to the bottom of the annulus (or drift wall).

4.3 Temperatures, Relative Humidities, and Vapor Mass Fractions Near the Heater

In this section, the temperature, relative humidity, and vapor mass fraction directly above and below the heater are plotted as a function of time during heating and cool-down for several simulations. The purpose is to gain insight into the temporal and spatial variation in these parameters under different heating conditions (constant heater temperature vs. constant heater output power) and environments (no annulus vs. annulus).

4.3.1 No Annulus (Simulation 1)

The temperatures, relative humidities, liquid saturations, and vapor mass fractions are uniformly distributed about the heater in this simulation (1) as a function of time, so the values at only one element (directly above the heater) are plotted as a function of time (Figure 4.8). The temperature of the element above the heater increases with time during heating as shown in Figure 4.8a. Subsequently, water is evaporated and the liquid saturation decreases as the vapor mass fraction increases. The water vapor moves outwards towards the constant temperature boundaries via concentration and pressure gradients. At around 2000 seconds, the liquid saturation goes to zero and the relative humidity and vapor mass fraction begin to decrease since no more water is being added to the gas phase in the element by evaporation. At this time, the temperature increases sharply as a result of less energy being used to evaporate the liquid water in that element. The relative humidity continues to decrease as the temperature increases.

Figure 4.8b shows the same variables plotted as a function of time during the cool-down period following 1 day of heating. To simulate the cool-down period, the heating element was physically removed from the model domain. The temperature gradually decreases until it reaches the ambient temperature near 20°C. The relative humidity increases at the same rate until it reaches a value of one. The vapor mass fraction decreases after 100 seconds of cool-down as air diffuses back towards the center of the tuff slab from the surrounding areas. Liquid water eventually returns to the element at the end of the cool-down period as evidenced by the increase in liquid saturation.

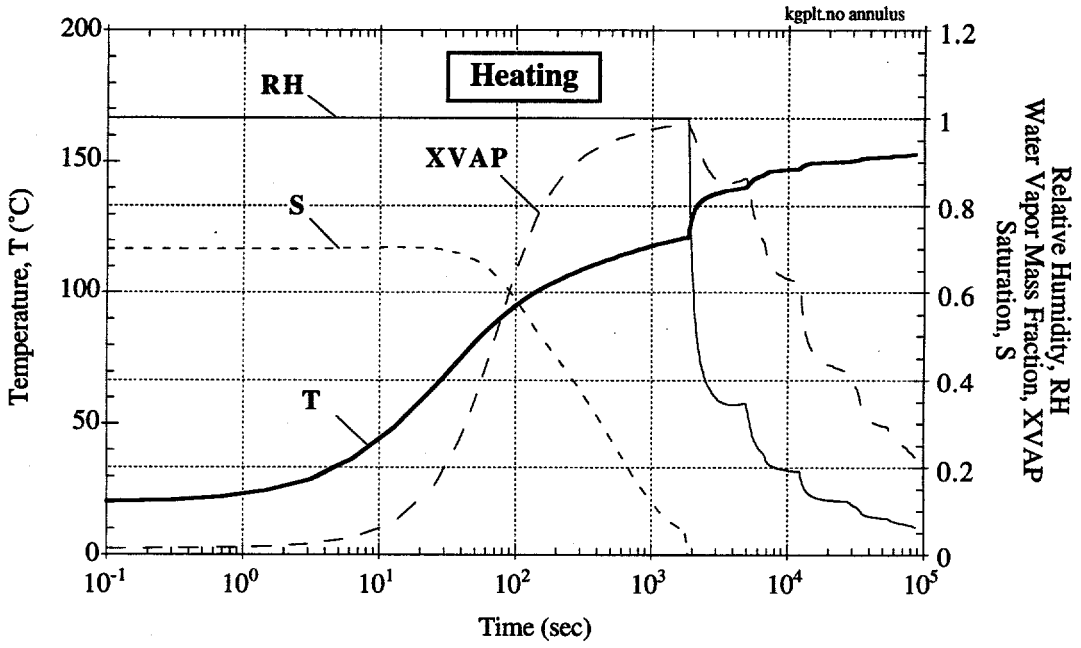

(a)

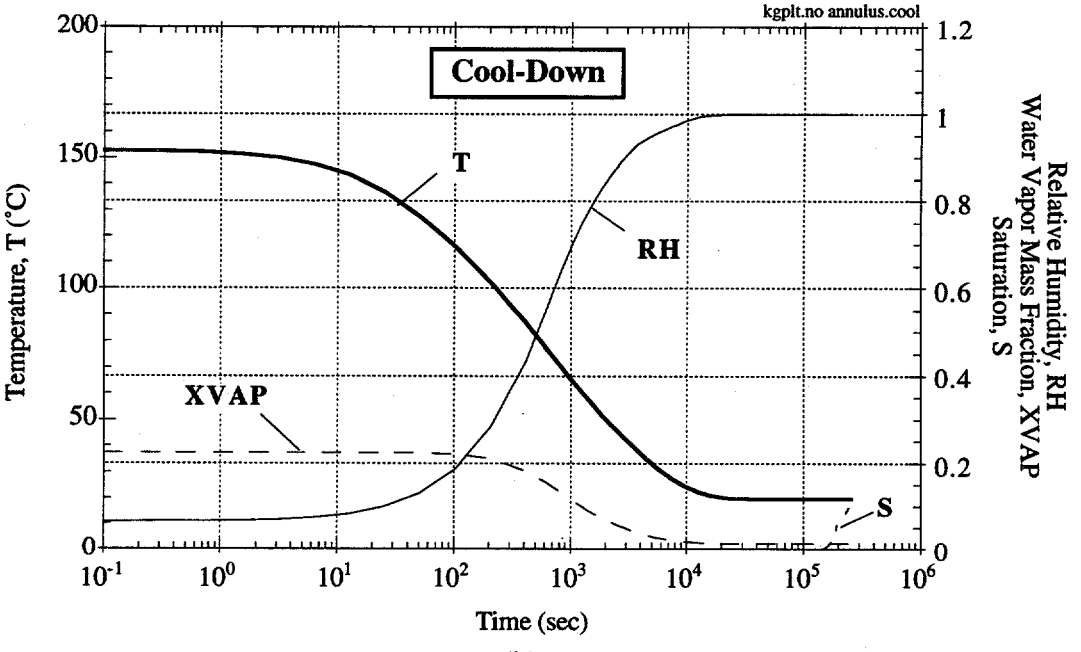

(b)

Figure 4.8. Temperature, relative humidity, vapor mass fraction, and liquid saturation as a function of time during (a) heating and (b) cool-down for the element directly above the heater in simulation 1 with no annulus and a constant heater temperature of 200°C.

4.3.2 Sand Annulus (Simulation 3B and 3D)

The temperature, relative humidity, and vapor mass fraction are plotted as a function of time during heating for simulations 3B (constant heater temperature = 200°C) and 3D (constant heater power = 5W) in with a sand-filled annulus (Figure 4.9a&b). The permeability of the sand-filled annulus is low enough such that convection does not play a significant role in the thermohydrologic behavior of the system as noted in Figure 4.4. Thus, the variables above and below the heater are nearly identical during the entire heating period. The relative humidity decreases in the constant heater temperature case (3B) at first, but then rises to a steady value near 0.03 after 10^4 seconds (Figure 4.9a). The constant heater power simulation shows a steady decrease in the relative humidity to near the same value of 0.03 after 10^4 seconds with no significant increase. Perhaps the more rapid increase in temperature in the constant heater temperature case caused the sharp drop in the relative humidities. As the rate of temperature rise decreased, the relative humidity began to slowly increase as vapor diffused towards the heater from the surrounding wet tuff slab. The vapor mass fraction behaves similarly in both simulations, rising gradually to a steady value as vapor diffuses towards the heater. After 10^4 seconds, the simulations show a quasi-steady condition in which the variables are relatively constant with time. It should be noted that the constant heater temperature simulation (3B) produces a heater output that is slightly higher than 5 W during the quasi-steady condition, so the quasi-steady temperatures are expected to be higher.

Figure 4.10 shows the cool-down behavior of these systems is very similar following one day of heating. The temperatures and vapor mass fractions gradually decrease with a subsequent rise in the relative humidity. Ambient conditions are reached after 10^4 seconds of cool-down.

4.3.3 Air Annulus (Simulation 2C and 2D)

The heating behavior of a system with a simulated air annulus is quite different between simulations using a constant heater temperature of 200°C (2C) and a constant heater power of 5 W (2D). Figure 4.11a shows that because of the small heat capacity of the air in the annulus, a constant heater temperature immediately increases the temperature of the air near the heater. On the other hand, a constant heater power requires a longer time to heat the air elements next to the heater. In both cases, the higher permeability of the air elements in these simulations allows a significant amount of convection to occur in the annulus. As a result, the temperatures and relative humidities are noticeably different between the elements above and below the heater. Figure 4.11a shows that the relative humidity again decreases rapidly in the constant heater temperature simulation and gradually rises to a steady-value as vapor diffuses towards the heater from the

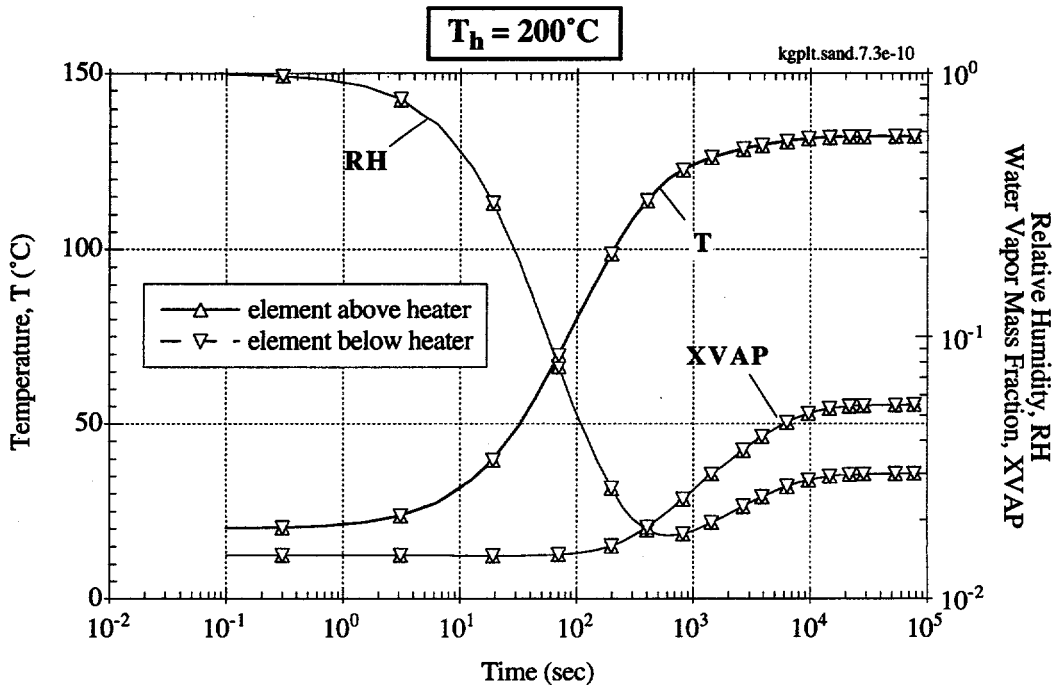

(a)

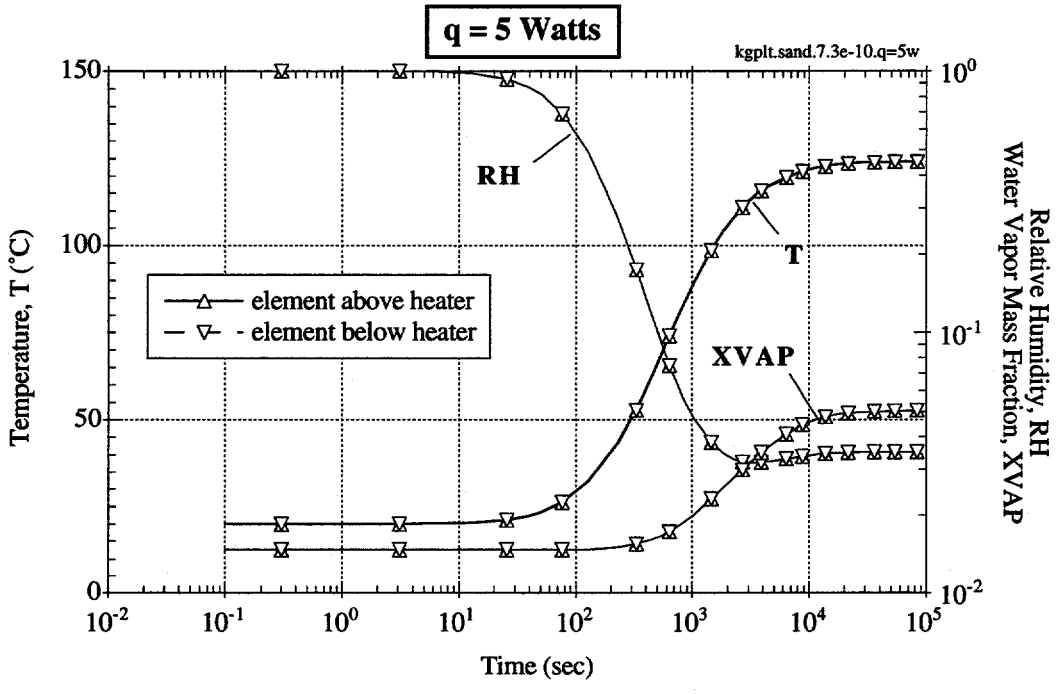

(b)

Figure 4.9. Temperature, relative humidity, and vapor mass fraction plotted as a function of time during (a) constant temperature heating and (b) constant power heating for the elements directly above and below the heater in simulations 3B and 3D with a sand annulus.

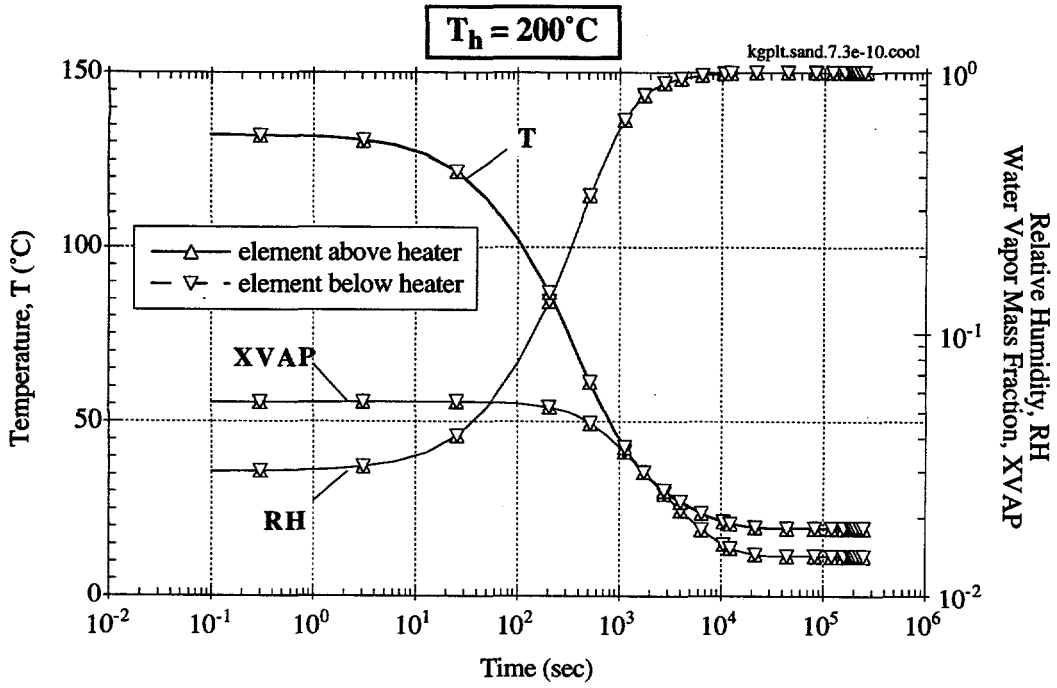

(a)

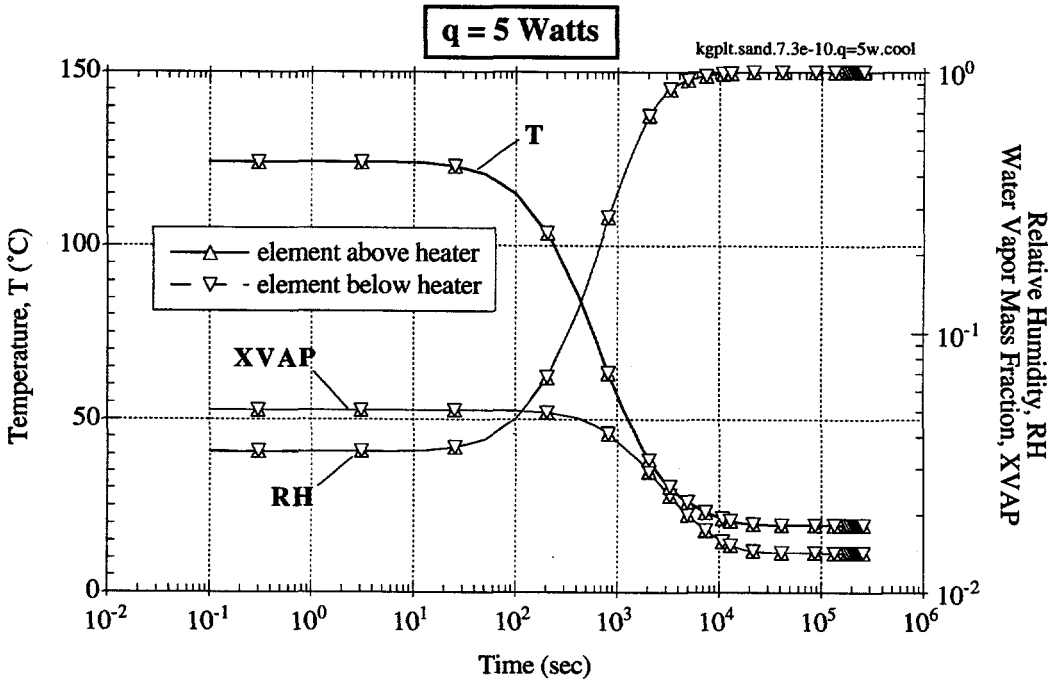

(b)

Figure 4.10. Temperature, relative humidity, and vapor mass fraction plotted as a function of time during cool-down following (a) constant temperature heating and (b) constant power heating for the elements directly above and below the heater in simulations 3B and 3D with a sand annulus.

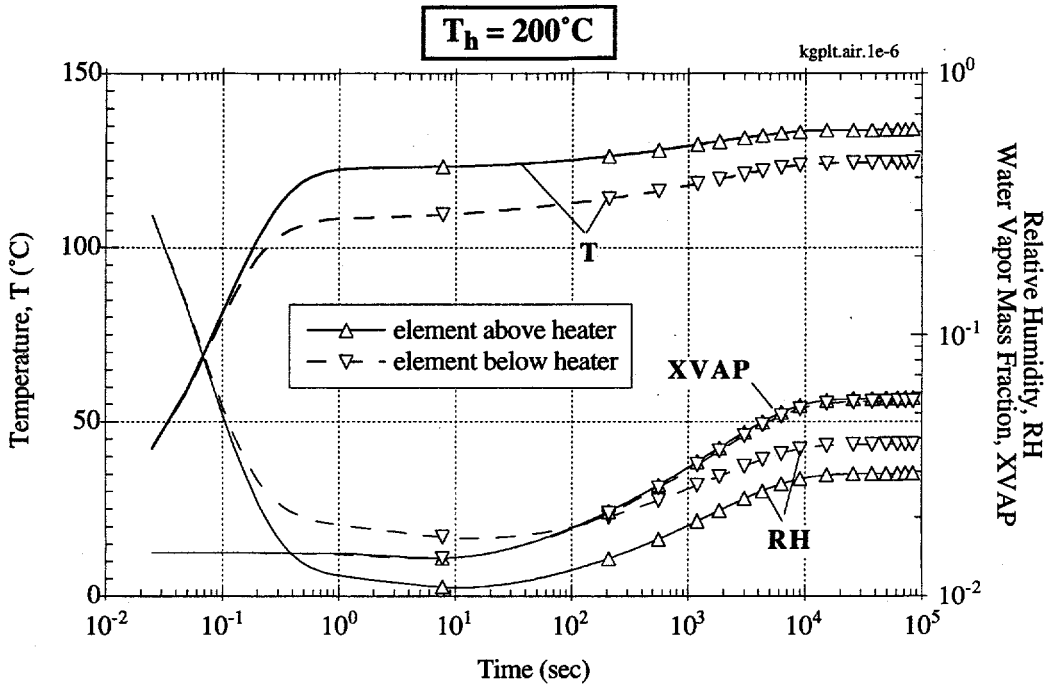

(a)

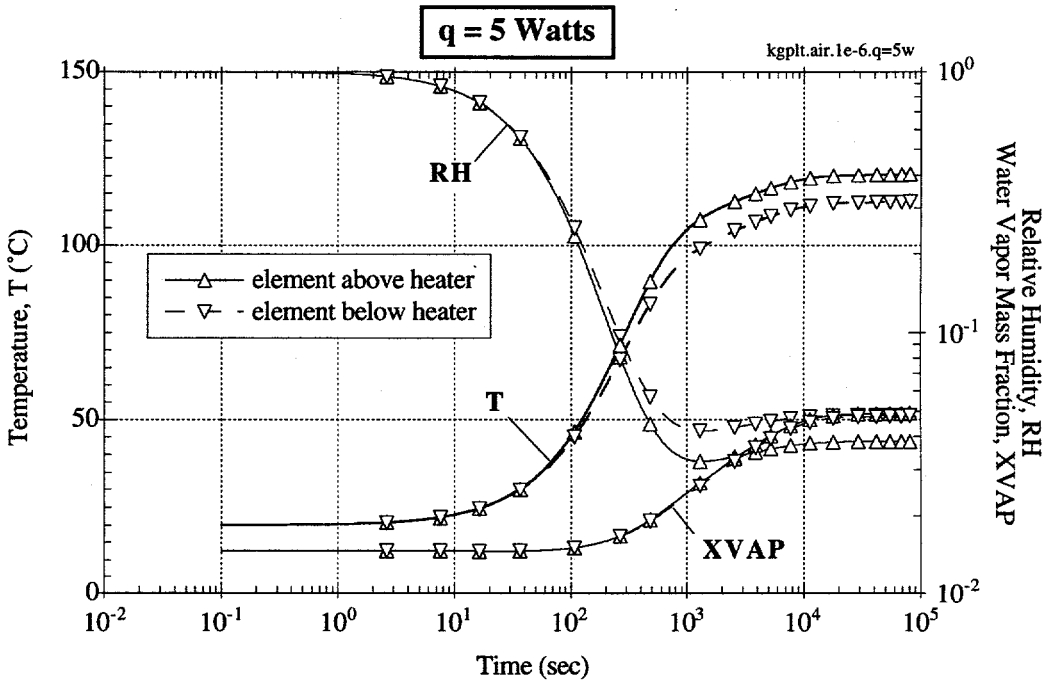

(b)

Figure 4.11. Temperature, relative humidity, and vapor mass fraction plotted as a function of time during (a) constant temperature heating and (b) constant power heating for the elements directly above and below the heater in simulations 2D and 2E with an air annulus.

surrounding wet tuff slab. Quasi-steady conditions are again reached after approximately 10^4 seconds of heating. An interesting point to note in this plot is that although the temperatures (and hence relative humidities) vary between the elements just above and below the heater, the vapor mass fractions are the same.

Figure 4.12a shows that as soon as the heater element is removed from the system after one day of constant temperature heating, the temperature drops rapidly while the relative humidity increases at the same rate. This is in contrast to the cool-down behavior following one-day of constant power heating (Figure 4.12b). The temperature takes a longer time to begin cooling down in the presence of the heater, which is still present but turned off. Recall that in the constant temperature heating simulations, cool-down was simulated by removing the heater. In the constant power heating simulations, cool-down was simulated by simply turning the power off but leaving the heater element in place. In the previous sections (4.2.1 and 4.2.2), the method of cooling did not affect the cool-down behavior significantly because the material of the elements next to the heater had similar heat capacities to that of the heater. Thus, even though the heater was removed in those previous simulations, the elements next to the heater remained hot. In this simulation, however, the air elements next to the heater quickly dissipate their energy once the heater is removed from the system. Nevertheless, both simulations reach ambient conditions after 10^4 seconds of cooling.

4.4 Quantification of the Significance of Convection on Thermohydrologic Parameters

The significance of convection evidenced in several of the simulations presented earlier can be quantified by determining several non-dimensional parameters defined in section 3.2.4 and 3.2.5. The Nusselt number is plotted against the Rayleigh-Darcy number in Figure 4.13 for all the simulations listed in Table 4.1 with an annulus to show the effects of convection. As the Rayleigh-Darcy number increases beyond a value of 10, the Nusselt number begins to increase according to the power law expression given in the bottom plot in Figure 4.13. The Rayleigh-Darcy number gives a measure of the buoyancy to viscous forces in the annulus and depends strongly on the permeability of the annulus as defined in equation (3.10). As the permeability of the annulus increases, the convection becomes more significant and the heat transfer by convection is enhanced as evidenced by the increasing Nusselt numbers. It should be noted that the Nusselt and Rayleigh-Darcy numbers were calculated at quasi-steady conditions of heating ($t=8.64 \times 10^4$ seconds). Therefore, the correlation shown in Figure 4.13 is independent of the backfill material since the heat capacity of the solid phase drops out of the energy equation under steady conditions.

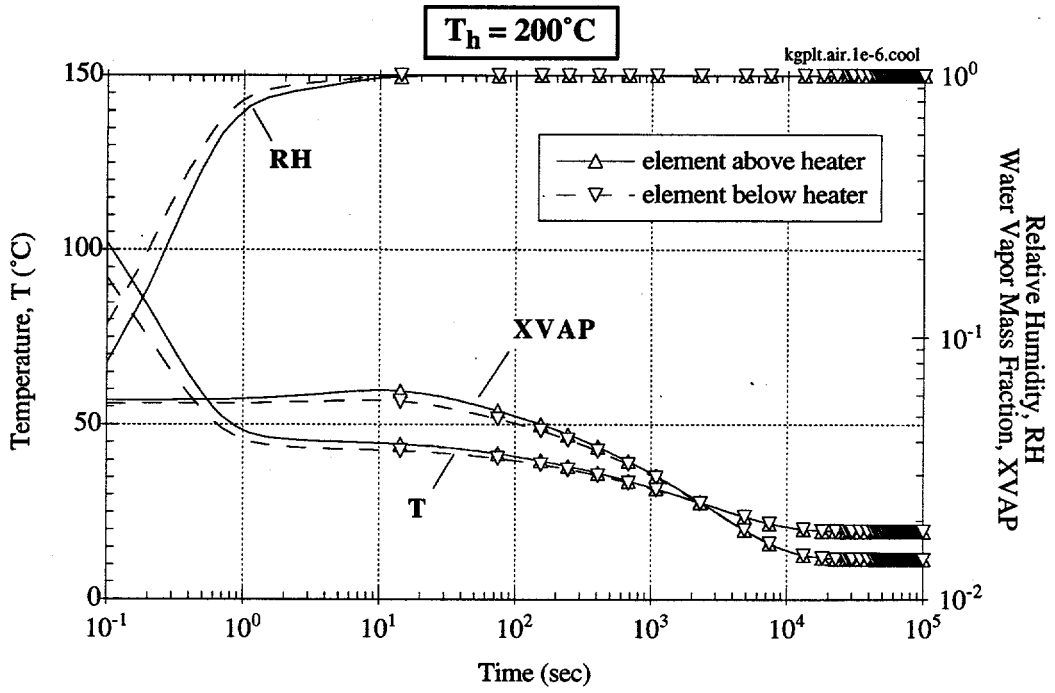

(a)

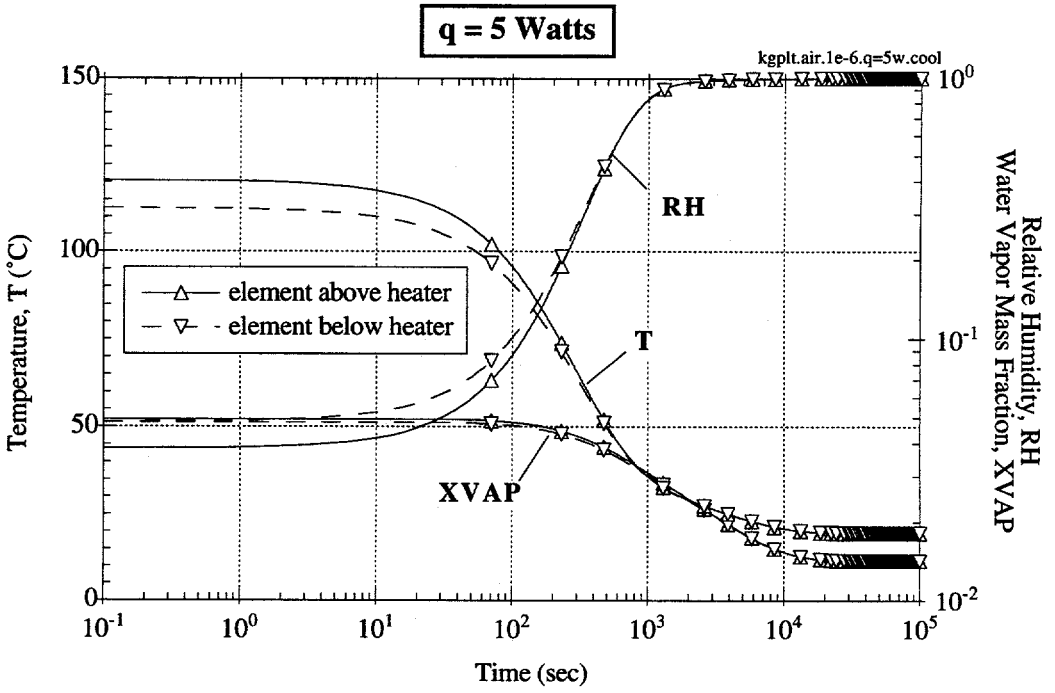

(b)

Figure 4.12. Temperature, relative humidity, and vapor mass fraction plotted as a function of time during cool-down following (a) constant temperature heating and (b) constant power heating for the elements directly above and below the heater in simulations 2D and 2E with an air annulus.

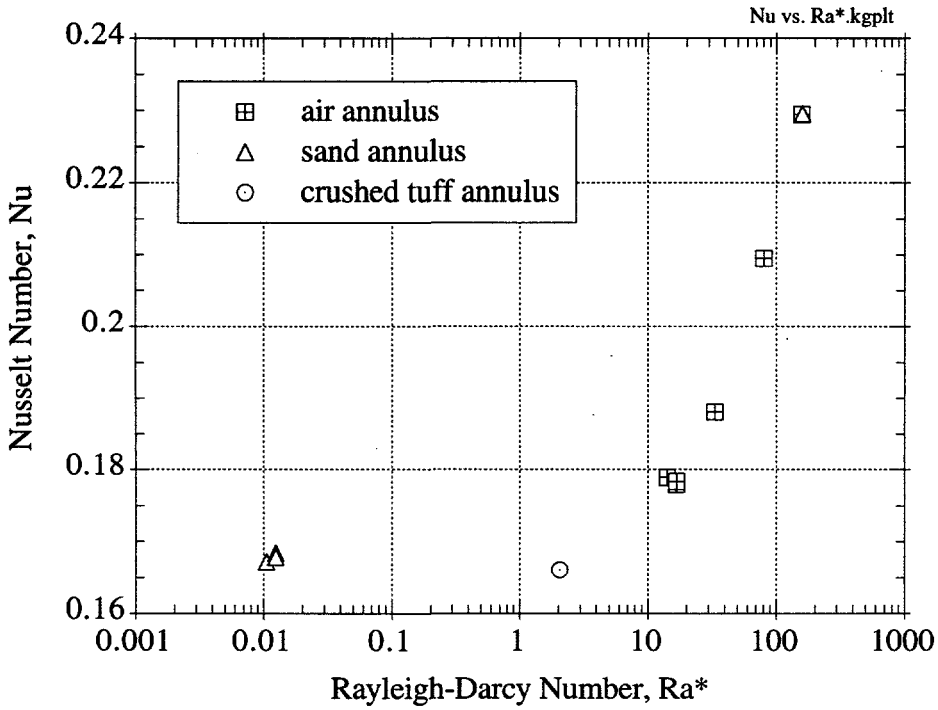

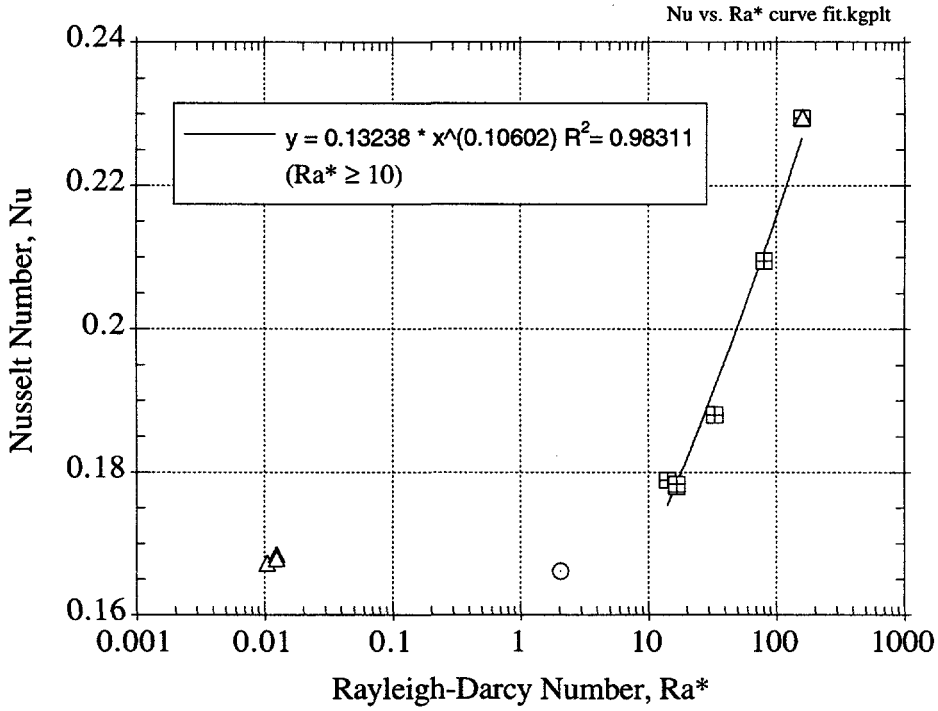

Figure 4.13. Nusselt number as a function of the Rayleigh-Darcy number for different backfill materials in the annulus of the heater experiment. The bottom plot shows a power law curve fit for Ra* ≥ 10.

Another indicator of the significance of convection is the variation in temperature and relative humidity near the heater. If convection is significant, the temperatures above the heater should be higher than the temperatures below the heater as a result of the convective cells that develop in the annulus. Hot air rises upward from the heater where it circulates around the outside of the annulus, cooling towards the bottom. Figure 4.14 plots the variation in the temperature and relative humidity directly above and below the heater as defined in equations 3.12 and 3.13. As the Rayleigh-Darcy number increases beyond a value of 10, the variations in both parameters increase significantly. Although the Rayleigh-Darcy number used in these laboratory-scale simulations may not correspond to the equivalent Rayleigh-Darcy number in drift-scale simulations because of the different length scales (L_c), similar behavior should occur regardless of scale. Beyond a critical Rayleigh-Darcy number, the Nusselt number, as well as the variations in temperature and relative humidity, will increase significantly. These convective altered environments may impact the containment-performance of the waste packages.

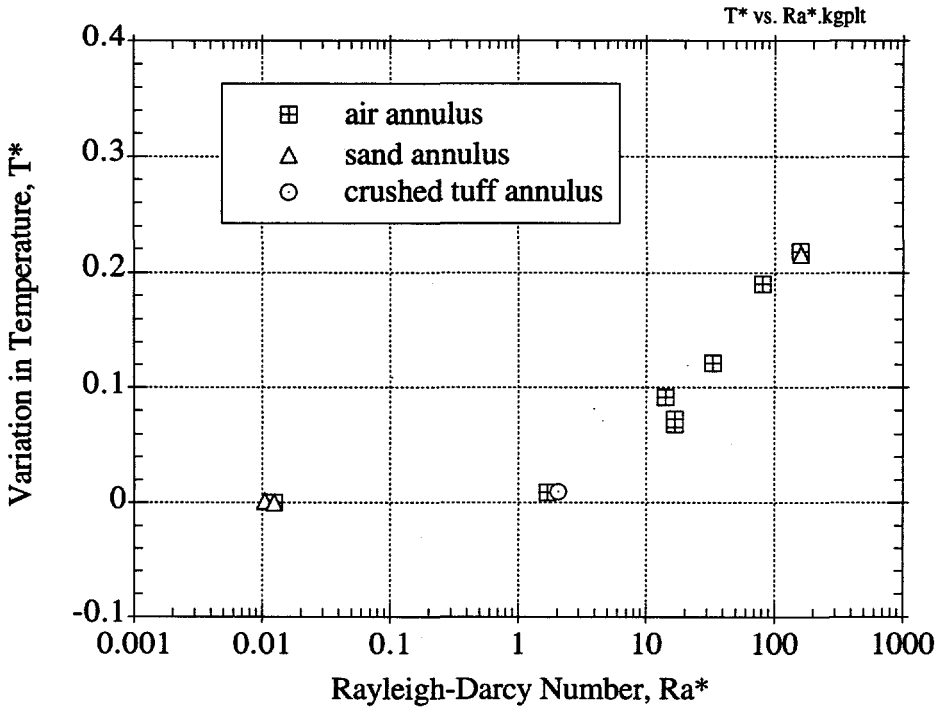

(a)

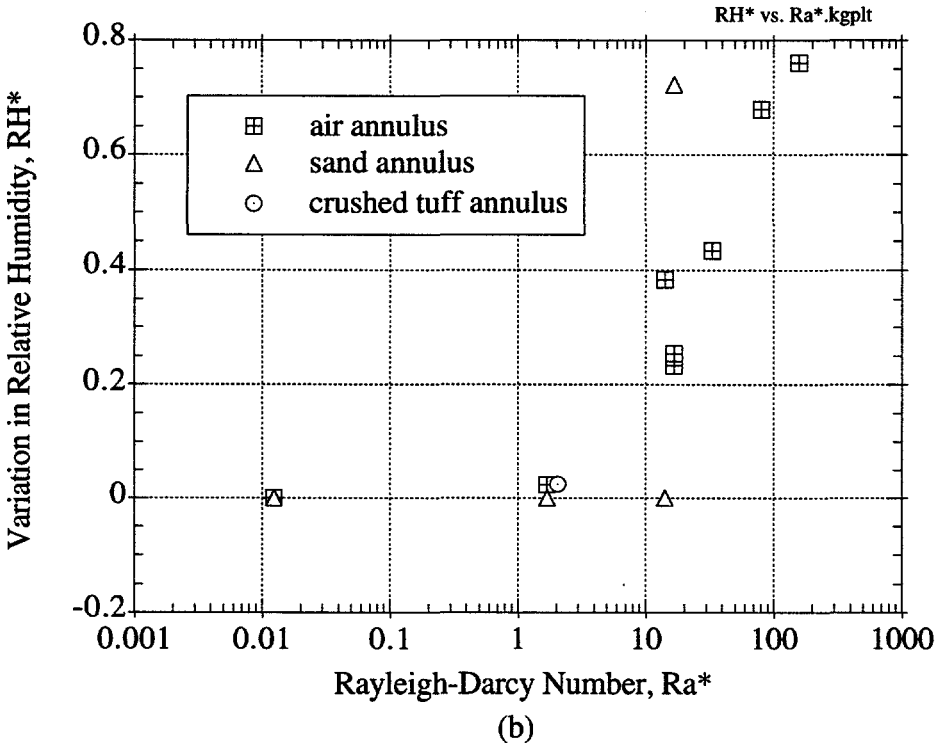

(b)

Figure 4.14. Variations in a) temperature and b) relative humidity near the heater as a function of the Rayleigh-Darcy number for different backfill materials in the annulus. The variation is calculated as the difference between two values directly above and below the heater divided by the mean of those two values.

Chapter

FIVE

Conclusions and Recommendations

Laboratory-scale heater tests have been proposed to investigate thermohydrologic processes in actual tuffaceous rock surrounding a heat source. These experiments are designed to gain insight and aid in the understanding of thermohydrologic behavior that may exist at the potential repository at Yucca Mountain, Nevada, once heat-generating wastes are emplaced. Based on numerical pre-test simulations of these heater experiments, the following conclusions and recommendations are made:

- The heat transfer through the annulus (or drift) can be significantly enhanced by convection when the Rayleigh-Darcy number exceeds a critical value (=10 in the laboratory experiments). In addition, significant variations in the temperature and relative humidity can exist near the heater under these conditions.

- The Rayleigh-Darcy number depends strongly on the permeability within the annulus (or drift) as well as the effective thermal conductivity. More simulations should be conducted at the field-scale to determine more precise relationships between non-dimensional parameters governing convection on the drift scale.

- Drying occurs preferentially near the top of the annulus (or drift) when convection is important. Redistribution of the moisture from the top of the annulus (or drift) to the bottom may result from the following processes at early times: 1) hot air flowing upward from the heater evaporates liquid from the top of the annulus (or drift) and 2) subsequent condensation occurs from the cooling air flowing downward along the outside of the annulus (or drift) to the bottom.

- A heater power of 5 Watts is similar to a constant heater temperature of 200°C under quasi-steady heating conditions in the simulated experiments. If heat loss is present in the actual experiments, the heater power may need to be increased.

- Noticeable saturation variations and drying occur in the tuff slab within one day of simulated heating at a heater temperature of 200°C or a heater power of 5 Watts. Ambient conditions in the elements directly above and below the heater are reached within one day of simulated cooling.

- Radiation should be explicitly modeled to determine its relative contribution to heat transfer within the annulus (or drift).

- Laboratory-scale heater experiments should be performed to verify the assertions and hypotheses presented in this report. Laboratory data can also be used to infer information about the effective permeability in the annulus and the relative contribution from radiation.

- Simulations and future experiments should consider the effects of fractures on the thermohydrologic behavior around a heater.

Chapter
SIX

References

Basel, M.D. and K.S. Udell, 1991, Effect of Heterogeneities on the Shape of Condensation Fronts in Porous Media, *Heat Transfer in Geophysical Media*, ASME HTD-Vol. 172, American Society of Mechanical Engineers, pp. 63-70.

Buscheck, T.A. and J.J. Nitao, 1993, The Analysis of Repository-Heat-Driven Hydrothermal Flow at Yucca Mountain, in *Proceedings of the 4th International High Level Radioactive Waste Management Conference*, Las Vegas, NV, pp. 847-867.

Chen, Y.-T., D. Manuel, and R. Boehm, 1995, Unsaturated Flows in a Porous Medium Containing a Heated Air Annulus, in *Proceedings of the Sixth International High Level Radioactive Waste Management Conference*, Las Vegas, NV, pp. 349-351.

Gansemer J.D. and A. Lamont, 1995, Effect of Areal Power Density and Relative Humidity on Corrosion Resistant Container Performance, in *Proceedings of the Sixth International High Level Radioactive Waste Management Conference*, Las Vegas, NV, pp. 313-315.

Glass, R.J., V.C. Tidwell, A.L. Flint, W. Peplinski, and Y. Castro, 1994, Fracture-Matrix Interaction in Topopah Spring Tuff: Experiment and Numerical Analysis, in *Proceedings of the Fifth International High Level Radioactive Waste Management Conference*, Las Vegas, NV, pp. 1905-1914.

Ho, C.K. and R.R. Eaton, 1994, Studies of Thermohydrologic Flow Processes Using TOUGH2, SAND94-2011, Sandia National Laboratories, Albuquerque, NM.

Ho, C.K., K.S. Maki, and R.J. Glass, 1994, Studies of Non-Isothermal Flow in Saturated and Partially Saturated Porous Media, SAND93-4045C, in *Proceedings of the Fifth International High Level Radioactive Waste Management Conference*, Las Vegas, NV, pp. 2481-2491.

Incropera, F. P. and D. P. De Witt, 1985, *Introduction to Heat Transfer*, John Wiley & Sons, New York.

Izzeldin, A., E. Hanson, and R. Boehm, 1994, Unsaturated Flow Experiment with Phase Change—The Heat Pipe Effect, in *Proceedings of the Fifth International High Level Radioactive Waste Management Conference*, Las Vegas, NV, pp. 2475-2480.

Jury, W.A. and J. Letey, Jr., 1979, Water Vapor Movement in Soil: Reconciliation of Theory and Experiment, *Soil Science Society of America Journal*, Vol. 43, No. 5, pp. 823-827.

Manteufel, R.D. and R.T. Green, 1993, Observations of Thermally-Driven Liquid Redistribution in a Partially Saturated Porous Medium, *Multiphase Transport in Porous Media*, FED-Vol. 173/HTD-Vol. 265, American Society of Mechanical Engineers, New York, pp. 93-107.

McNeish, J.A. M. Reeves, T.F. Dale, and R.W. Andrews, 1995, Preliminary Evaluation of Waste Package Releases Using Drfit-Scale Thermo-Hydrologic Analyses, in *Proceedings of the Sixth International High Level Radioactive Waste Management Conference*, Las Vegas, NV, pp. 319-322.

Nield, D.A. and A. Bejan, 1992, *Convection in Porous Media*, Springer-Verlag, New York.

Pruess, K., 1991, TOUGH2—A General-Purpose Numerical Simulator for Multiphase Fluid and Heat Flow, LBL-29400, Lawrence Berkeley Laboratory, Berkeley, CA.

Pruess, K., 1987, TOUGH User's Guide, SAND86-7104, NUREG/CR-4645, LBL-20700, Lawrence Berkeley Laboratory, Berkeley, CA.

Pruess, K. and Y. Tsang, 1994, Thermal Modeling for a Potential International High Level Nuclear Waste Repository at Yucca Mountain, Nevada, LBL-35381, Lawrence Berkeley Laboratory, Berkeley, CA.

Pruess, K. and Y. Tsang, 1993, Modeling of Strongly Heat-Driven Flow Processes at a Potential International High Level Nuclear Waste Repository, at Yucca Mountain, Nevada, in *Proceedings of the Fourth International High Level Radioactive Waste Management Conference*, Las Vegas, NV, pp. 568-575.

Pruess, K., J.S.Y. Wang, and Y.W. Tsang, 1990, On Thermohydrologic Conditions Near International High Level Nuclear Wastes Emplaced in Partially Saturated Fractured Tuff. 1. Simulation Studies With Explicit Consideration of Fracture Effects, *Water Resources Research*, Vol. 26, No. 6, pp. 1235-1248.

Ramirez, A.L., T.A. Buscheck, R. Carlson, W. Daily, V.R. Latorre, K. Lee, W. Lin, N. Mao, D. Towse, T. Ueng, and D. Watwood, 1990, Prototype Heater Test of the Environment Around a Simulated Waste Package, *Proceedings of the International Topical Meeting on High Level Radioactive Waste Management Conference*, Las Vegas, NV, pp. 870-881.

Tidwell, V.C. and R.J. Glass, 1992, X-Ray and Visible Light Transmission as Two-Dimensional, Full-Field Moisture-Sensing Techniques: A Preliminary Comparison, in *Proceedings of the Third International High Level Radioactive Waste Management Conference*, Las Vegas, NV, pp. 1099-1110.

Tsang, Y. W. and K. Pruess, 1987, A Study of Thermally Induced Convection Near a International High Level Nuclear Waste Repository in Partially Saturated Fractured Tuff, LBL-21311, SAND86-7010J, *Water Resources Research*, **23**(10), pp. 1958-1966.

van Genuchten, M. Th., 1980, A Closed-Form Equation for Predicting the Hydraulic Conductivity of Unsaturated Soils, *Soil Sci. Soc. Am. J.*, Vol. 44, pp. 892-898.

Wilson, M.L., J.H. Gauthier, R.W. Barnard, G.E. Barr, H.A. Dockery, E. Dunn, R.R. Eaton, D.C. Guerin, N. Lu, M.J. Martinez, R. Nilson, C.A. Rautman, T.H. Robey, B. Ross, E.E. Ryder, A.R. Schenker, S.A. Shannon, L.H. Skinner, W.G. Halsey, J. Gansemer, L.C. Lewis, A.D. Lamont, I.R. Triay, A. Meijer, and D.E. Morris, 1994, Total-System Performance Assessment for Yucca Mountain—SNL Second Iteration (TSPA-1993), SAND93-2675, Sandia National Laboratories, Albuquerque, NM.

Appendix

A

RIB Information

Information from the Reference Information Base Used in this Report

This report contains no information from the Reference Information Base.

Candidate Information for the Reference Information Base

This report contains no candidate information for the Reference Information Base.

Candidate Information for the Geographic Nodal Information Study and Evaluation System

This report contains no candidate information for the Geographic Nodal Information Study and Evaluation System.

YUCCA MOUNTAIN SITE CHARACTERIZATION PROJECT

UC814 - DISTRIBUTION LIST

1 D. A. Dreyfus (RW-1)
Director
OCRWM
US Department of Energy
1000 Independence Avenue SW
Washington, DC 20585

1 L. H. Barrett (RW-2)
Acting Deputy Director
OCRWM
US Department of Energy
1000 Independence Avenue SW
Washington, DC 20585

1 S. Rousso (RW-40)
Office of Storage and Transportation
OCRWM
US Department of Energy
1000 Independence Avenue SW
Washington, DC 20585

1 R. A. Milner (RW-30)
Office of Program Management
and Integration
OCRWM
US Department of Energy
1000 Independence Avenue SW
Washington, DC 20585

1 D. R. Elle, Director
Environmental Protection Division
DOE Nevada Field Office
US Department of Energy
P.O. Box 98518
Las Vegas, NV 89193-8518

1 T. Wood (RW-14)
Contract Management Division
OCRWM
US Department of Energy
1000 Independence Avenue SW
Washington, DC 20585

4 Victoria F. Reich, Librarian
Nuclear Waste Technical Review Board
1100 Wilson Blvd., Suite 910
Arlington, VA 22209

5 Wesley Barnes, Project Manager
Yucca Mountain Site Characterization
Office
US Department of Energy
P.O. Box 98608--MS 523
Las Vegas, NV 89193-8608

1 Director
Office of Public Affairs
DOE Nevada Operations Office
US Department of Energy
P.O. Box 98518
Las Vegas, NV 89193-8518

8 Technical Information Officer
DOE Nevada Operations Office
US Department of Energy
P.O. Box 98518
Las Vegas, NV 89193-8518

1 P. K. Fitzsimmons, Technical Advisor
Office of Assistant Manager for
Environmental Safety and Health
DOE Nevada Operations Office
US Department of Energy
P.O. Box 98518
Las Vegas, NV 89193-8518

1 J. A. Blink
Deputy Project Leader
Lawrence Livermore National Laboratory
101 Convention Center Drive
Suite 820, MS 527
Las Vegas, NV 89109

2 J. A. Canepa
Technical Project Officer - YMP
N-5, Mail Stop J521
Los Alamos National Laboratory
P.O. Box 1663
Los Alamos, NM 87545

1 Repository Licensing & Quality
Assurance
Project Directorate
Division of Waste Management
US NRC
Washington, DC 20555

1 Senior Project Manager for Yucca
Mountain
Repository Project Branch
Division of Waste Management
US NRC
Washington, DC 20555

1 NRC Document Control Desk
Division of Waste Management
US NRC
Washington, DC 20555

1 Chad Glenn
NRC Site Representative
301 E Stewart Avenue, Room 203
Las Vegas, NV 89101

1 E. P. Binnall
Field Systems Group Leader
Building 50B/4235
Lawrence Berkeley Laboratory
Berkeley, CA 94720

1 Center for Nuclear Waste
Regulatory Analyses
6220 Culebra Road
Drawer 28510
San Antonio, TX 78284

2 W. L. Clarke
Technical Project Officer - YMP
Attn: YMP/LRC
Lawrence Livermore National Laboratory
P.O. Box 5514
Livermore, CA 94551

1 V. R. Schneider
Asst. Chief Hydrologist -- MS 414
Office of Program Coordination
and Technical Support
US Geological Survey
12201 Sunrise Valley Drive
Reston, VA 22092

1 J. S. Stuckless, Chief
Geologic Studies Program
MS 425
Yucca Mountain Project Branch
US Geological Survey
P.O. Box 25046
Denver, CO 80225

1 N. Z. Elkins
Deputy Technical Project Officer
Los Alamos National Laboratory
Mail Stop 527
101 Convention Center Drive, #820
Las Vegas, NV 89109

2 Michaele C. Brady
Technical Project Officer - YMP
Sandia National Laboratories
Organization 6302, MS 1399
101 Convention Center Drive, Suite 880
Las Vegas, NV 89109

1 Ray Wallace
US Geological Survey
106 National Center
12201 Sunrise Valley Drive
Reston, VA 22092

1 L. R. Hayes
Technical Project Officer
Yucca Mountain Project Branch
MS 425
US Geological Survey
P.O. Box 25046
Denver, CO 80225

1 A. L. Flint
US Geological Survey
MS 721
P.O. Box 327
Mercury, NV 89023

1 R. E. Lewis
Yucca Mountain Project Branch
MS 425
US Geological Survey
P.O. Box 25046
Denver, CO 80225

1 D. Zesiger
US Geological Survey
101 Convention Center Drive
Suite 860, MS 509
Las Vegas, NV 89109

2 L. D. Foust
Nevada Site Manager
TRW Environmental Safety Systems
101 Convention Center Drive
Suite P-110, MS 423
Las Vegas, NV 89109

1 C. E. Ezra
YMP Support Office Manager
EG&G Energy Measurements Inc.
MS V-02
P.O. Box 1912
Las Vegas, NV 89125

1 E. L. Snow, Program Manager
Roy F. Weston, Inc.
955 L'Enfant Plaza SW
Washington, DC 20024

1 Technical Information Center
Roy F. Weston, Inc.
955 L'Enfant Plaza SW
Washington, DC 20024

1 Technical Project Officer - YMP
US Bureau of Reclamation
Code D-3790
P.O. Box 25007
Denver, CO 80225

1 B. T. Brady
Records Specialist
US Geological Survey
MS 421
P.O. Box 25046
Denver, CO 80225

1 M. D. Voegele
Technical Project Officer - YMP
M&O/SAIC
101 Convention Center Drive
Suite 407
Las Vegas, NV 89109

1 Paul Eslinger, Manager
PASS Program
Pacific Northwest Laboratories
P.O. Box 999
Richland, WA 99352

1 A. T. Tamura
Science and Technology Division
OSTI
US Department of Energy
P.O. Box 62
Oak Ridge, TN 37831

1 P. J. Weeden, Acting Director
Nuclear Radiation Assessment Div.
US EPA
Environmental Monitoring Sys. Lab
P.O. Box 93478
Las Vegas, NV 89193-3478

1 ONWI Library
Battelle Columbus Laboratory
Office of Nuclear Waste Isolation
505 King Avenue
Columbus, OH 43201

1 C. H. Johnson
Technical Program Manager
Agency for Nuclear Projects
State of Nevada
Evergreen Center, Suite 252
1802 N. Carson Street
Carson City, NV 89710

1 John Fordham, Deputy Director
Water Resources Center
Desert Research Institute
P.O. Box 60220
Reno, NV 89506

1 The Honorable Cyril Schank
Chairman
Churchill County Board of
Commissioners
190 W. First Street
Fallon, NV 89406

1 T. Hay, Executive Assistant
Office of the Governor
State of Nevada
Capitol Complex
Carson City, NV 89710

3 R. R. Loux
Executive Director
Agency for Nuclear Projects
State of Nevada
Evergreen Center, Suite 252
1802 N. Carson Street
Carson City, NV 89710

1 Brad R. Mettam
Inyo County Yucca Mountain
Repository Assessment Office
P. O. Drawer L
Independence, CA 93526

1 Lander County Board of Commissioners
315 South Humbolt Street
Battle Mountain, NV 89820

1 Vernon E. Poe
Office of Nuclear Projects
Mineral County
P.O. Box 1600
Hawthorne, NV 89415

1 Les W. Bradshaw
Program Manager
Nye County Nuclear Waste Repository
Project Office
P.O. Box 1767
Tonopah, NV 89049

1 Florindo Mariani
White Pine County Coordinator
P. O. Box 135
Ely, NV 89301

1 Judy Foremaster
City of Caliente Nuclear Waste
Project Office
P.O. Box 158
Caliente, NV 89008

1 Philip A. Niedzielski-Eichner
Nye County Nuclear Waste
Repository Project Office
P.O. Box 221274
Chantilly, VA 22022-1274

1 Dennis Bechtel, Coordinator
Nuclear Waste Division
Clark County Department of
Comprehensive Planning
301 E. Clark Avenue, Suite 570
Las Vegas, NV 89101

1 Juanita D. Hoffman
Nuclear Waste Repository
Oversight Program
Esmeralda County
P.O. Box 490
Goldfield, NV 89013

1 Eureka County Board of Commissioners
Yucca Mountain Information Office
P.O. Box 714
Eureka, NV 89316

1 Economic Development Dept.
City of Las Vegas
400 E. Stewart Avenue
Las Vegas, NV 89101

1 Community Planning & Development
City of North Las Vegas
P.O. Box 4086
North Las Vegas, NV 89030

1 Community Development & Planning
City of Boulder City
P.O. Box 61350
Boulder City, NV 89006

1 Commission of European Communities
200 Rue de la Loi
B-1049 Brussels
BELGIUM

2 Librarian
YMP Research & Study Center
MS 407
P.O. Box 98521
Las Vegas, NV 89193-8521

1 Amy Anderson
Argonne National Laboratory
Building 362
9700 S. Cass Avenue
Argonne, IL 60439

1 Glenn Van Roekel
Director of Community Development
City of Caliente
P.O. Box 158
Caliente, NV 89008

1 G. S. Bodvarsson
Head, Nuclear Waste Department
Lawrence Berkeley Laboratory
1 Cyclotron Road, MS 50E
Berkeley, CA 94720

1 Michael L. Baughman
Intertech Services Corp.
P.O. Box 93537
Las Vegas, NV 89193

1 T. Buscheck
Lawrence Livermore National Laboratory
P. O. Box 808, L-206
Livermore, CA 94550

1 A. Wolfsberg
Los Alamos National Laboratory
EES-5, MS-F665
Los Alamos, NM 87545

1 Y. Tsang
Earth Sciences
Lawrence Berkeley Laboratory
1 Cyclotron Road, 50E
Berkeley, CA 94720

1 Y. Chen
UNLV
Department of Mechanical Engineering
4505 Maryland Parkway
Box 454027
Las Vegas, NV 89154-4027

1 B. Boehm, UNLV
UNLV
Department of Mechanical Engineering
4505 Maryland Parkway
Box 454027
Las Vegas, NV 89154-4027

1 Y. Xiang
INTERA, Inc.
TRW Environmental Safety Sys. Inc.
101 Convention Center Drive, Suite 110
Las Vegas, NV 89109

1 C. Li
INTERA, Inc.
101 Convention Center Drive
Las Vegas, NV 89109

1 M. Reeves
INTERA, Inc.
6850 Austin Center Blvd., Suite 300
Austin, TX 78731

1	S. Lingineni CRWMS/M&O 101 Convention Center Drive Las Vegas, NV 89109		MS	
		2	1330	C. B. Michaels, 6352 100/1.2.5.4.6/SAND95-1905/QA
		5	1330	WMT Library, 6352
1	R. W. Nelson INTERA, Inc. TRW Environmental Safety Sys. Inc. 101 Convention Center Drive, MS-425 Las Vegas, NV 89109	1	1326	H.A. Dockery, 6312
		1	1326	N.D. Francis, 6312
		1	1326	J.H. Gauthier, 6312
		1	1326	G.W. Perkins, 6312
		1	1326	M.L. Wilson, 6312
		1	1325	J. Pott, 6313
1	W. Zhou INTERA, Inc. 3609 South Wadsworth Blvd., #550 Denver, CO 80235	1	1325	L. S. Costin, 6313
		1	1325	R.E. Finley, 6313
		1	1325	E. Ryder, 6313
		1	1325	S.R. Sobolik, 6313
1	E. Smistad DOE 101 Convention Center Drive P200-216 Las Vegas, NV 89109	1	1324	P.B. Davies, 6115
		1	1324	R.J. Glass, 6115
		5	1324	C.K. Ho, 6115
		1	1324	V.C. Tidwell, 6115
		1	1324	S.W. Webb, 6115
1	Abe Van Luik 101 Convention Center Drive P200-219 Las Vegas, NV 89109	1	0827	M. Martinez, 1511
		1	0835	R.R. Eaton, 1511
1	R. Green CNWRA 6220 Culebra Road San Antonio, TX 78238-5166	1	MS 9018	Central Technical Files, 8523-2
		5	MS 0899	Technical Library, 13414
		1	MS 0619	Print Media, 12615
		2	MS 0100	Document Processing, 7613-2 for DOE/OSTI

Org.	Bldg.	Name	Rec'd by	Org.	Bldg.	Name	Rec'd by

Sandia National Laboratories